RESEARCH ARTICLE

Key Points:
- Normal stress and fluid pressure equally affect shear strength of calcite gouges at relatively low effective normal stresses (≤11 MPa)
- The degree of slip localization in calcite gouges sheared at seismic slip rates increases with effective normal stress
- Thermal pressurization has small effect on shear stress as it occurs after change from pressure- to temperature-controlled slip behavior

Correspondence to:
M. Rempe,
marieke.rempe@rub.de

Influence of Effective Stress and Pore Fluid Pressure on Fault Strength and Slip Localization in Carbonate Slip Zones

Marieke Rempe[1,2] ID, **Giulio Di Toro**[2,3] ID, **Thomas M. Mitchell**[4] ID, **Steven A. F. Smith**[5] ID, **Takehiro Hirose**[6] ID, **and Joerg Renner**[1]

[1]Institute for Geology, Mineralogy and Geophysics, Ruhr-Universitaet Bochum, Bochum, Germany, [2]Departimento die Geoscienze, Università degli Studi di Padova, Padua, Italy, [3]Instituti di Geofisica e Vulcanologia, INGV, Rome, Italy, [4]Rock and Ice Physics Laboratory and SeismoLab, Department of Earth Sciences, University College London, London, UK, [5]Department of Geology, University of Otago, Dunedin, New Zealand, [6]Kochi Institute for Core Sample Research, JAMSTEC, Kochi, Japan

Abstract The presence of pressurized fluids influences the mechanical behavior of faults. To test the roles of normal stress and fluid pressure on shear strength and localization behavior of calcite gouges, we conducted a series of rotary-shear experiments with pore fluid pressures up to 10.5 MPa and difference between normal stress and fluid pressure up to 11.2 MPa. Calcite gouges were sheared for displacements of 0.3 m to several meters at slip rates of 1 mm/s and 1 m/s. Drainage conditions in experiments were constrained from estimates of the hydraulic diffusivity. Gouges were found to be drained at 1 mm/s, but possibly partially undrained during sliding at 1 m/s. Shear strength obeys an effective-stress law with an effective-stress coefficient close to unity with a friction coefficient of ~0.7 that decreases to 0.19 due to dynamic weakening. The degree of comminution and slip localization constrained from experimental microstructures depends on the effective normal stress. Slip localization in calcite gouges does not occur at low effective normal stress. The presence of pore fluids lowers the shear strength of gouges sheared at 1 mm/s and causes an accelerated weakening at 1 m/s compared to dry gouges, possibly due to enhanced subcritical crack growth and intergranular lubrication. Thermal pressurization occurs only after dynamic weakening when friction is generally low and relatively independent of normal stress and therefore unaffected by thermal pressurization. The experimental results are consistent with the view that the presence of pressurized fluid in carbonate-bearing faults can facilitate earthquake nucleation.

1. Introduction

Many destructive earthquake ruptures nucleate within or propagate through carbonate rocks, for example, on faults in Italy (Chiarabba et al., 2009; Fondriest, 2014; Ventura & Di Giovambattista, 2013), and also in other areas worldwide (Delle Piane et al., 2017; Hartmann & Moosdorf, 2012). This seismicity in regions dominated by carbonate rocks has motivated a number of experimental studies aiming to understand the factors controlling the strength of faults in carbonates. Thus, a substantial amount of data on the frictional behavior of carbonate rocks has been collected in low-velocity (μm/s) to high-velocity (m/s) friction experiments, including tests on dry and saturated samples of cohesive carbonate rocks and carbonate-rich gouges (Rempe et al., 2017; Verberne et al., 2014; Violay et al., 2013, 2014). Accurately determining fault strength in frictional sliding experiments where fluids are present requires measurement of the local pore fluid pressure (Brantut, 2020; Proctor et al., 2019) because it affects the effective stress. Generally, fluid pressure is supposedly known in low-velocity (~μm/s) experiments (Kurzawski et al., 2018; Scuderi & Collettini, 2016; Verberne, Plümper, et al., 2014) focusing on interseismic fault strength and conditions for instability. Due to the complexities of sealing sample assemblies at high velocities (>1 cm/s) (Violay et al., 2013, 2014), many high-velocity experiments investigating the coseismic stage of fault slip have been conducted at initially saturated conditions, but without any ability to control or measure fluid pressure during the course of the experiments.

Evidence for the development of high fluid pressures in natural fault zones is provided by vein networks, interpreted as sealed hydrofractures preserved in active and exhumed fault zones. The development of

hydrofractures requires that fluid pressure exceeds the least principal stress (Secor, 1965; in limestones: Bullock et al., 2014). Estimates of pore fluid pressures in fault zones at depth deduced from fault zone drilling or based on moment-magnitude scaling (Miller, 2002a, 2002b) also suggest that fluid pressures may reach lithostatic values. The aftershocks of the 1997 earthquake sequence at Umbria-Marche, Italy, which nucleated and propagated within carbonate rocks, are examples of the involvement of pressurized fluids in faulting, because they were likely driven by pressurized CO_2 released from depth (Miller, 2013; Miller et al., 2004).

To quantify the effect of fluid pressure on the strength of faults or any rock property, it is necessary to understand how the properties depend on effective normal stress, $\sigma_{\mathrm{eff}} = \sigma_{\mathrm{n}} - \alpha p_{\mathrm{f}}$, the weighted difference of normal stress σ_{n} and pore fluid pressure p_{f}. The unweighted difference, that is, $\alpha = 1$, is commonly addressed as Terzaghi stress, $\sigma_{\mathrm{T}} = \sigma_{\mathrm{n}} - p_{\mathrm{f}}$. The weighting coefficient α may take different values for different physical properties, such as bulk volume deformation (for which α is called Biot-Willis coefficient), permeability, or shear strength (Paterson & Wong, 2005). It is generally assumed that the effective-stress coefficient for friction is close to unity, that is, $\alpha \approx 1$ in the linear relation $\tau = \mu(\sigma_{\mathrm{n}} - \alpha p_{\mathrm{f}})$, where τ is the shear stress and μ the friction coefficient. To our knowledge, the effective-stress law has never been investigated for the shear strength of carbonate gouges. Previous low-velocity (~μm/s) laboratory studies investigating the effect of pore fluid pressure on the shear strength of prefaulted rocks and phyllosilicate-bearing gouges found that the effective-stress law generally holds for the sliding resistance with $\alpha \approx 1$ (Morrow et al., 1992). Cases of $\alpha \neq 1$ for friction were explained by (partially) undrained conditions, that is, a mismatch between fluid pressure inside and outside the sample, for example, due to sample compaction (Moore et al., 1984; Paterson & Wong, 2005), resulting in an erroneous calculation of effective stress. In fact, the main experimental challenge in the determination of α for strength measures lies in robustly constraining the drainage state, in particular since pore-pressure transients may occur due to pore-volume changes or thermal pressurization, that is, a fluid-pressure increase due to shear compaction/dilation and frictional heating, respectively (Lachenbruch, 1980; Sibson, 1973). Clarification of drainage is essential for unequivocally determining the sensitivity of frictional strength to fluid pressure that is expressed by the corresponding α. As such, the effective-stress coefficient α is also a direct measure of the potential sensitivity of frictional resistance to thermal pressurization. For $\alpha \rightarrow 0$, thermal pressurization has no influence on strength even if it occurs. Thermal pressurization is also ineffective for $\mu \rightarrow 0$, that is, for a very low friction coefficient, as shear stress loses its dependence on effective normal stress altogether.

Thermal pressurization has been evaluated in numerous experimental (Badt et al., 2020; Brantut et al., 2008; Chen et al., 2017; Ferri et al., 2010; Violay et al., 2015) and theoretical (Andrews, 2002; Mase & Smith, 1987; Platt et al., 2014; Rempel & Rice, 2006; Rice, 2006) studies. Modeling results of Rice (2006) suggest that thermal pressurization of granular material during seismic slip may be an efficient weakening mechanism. Recent experiments have shown that thermal pressurization may occur even during shearing of rocks at relatively low velocity (mm/s), if conditions are undrained (Badt et al., 2020). Previous experimental studies on cohesive carbonate rocks, however, suggest that thermal pressurization plays a negligible role in their dynamic weakening, which is presumably governed by brittle failure of asperities, enhanced by subcritical crack growth and hydrolytic weakening (Violay et al., 2013, 2015). The effect of pore pressure on the mechanical behavior of noncohesive carbonate powders has not been studied at sufficient detail, despite its importance for interpreting the observed natural seismicity associated with mature fault zones that developed a layer of gouge in the fault core. In gouges, slip is not localized at the beginning of sliding (Rempe et al., 2017; Smith et al., 2015). The microstructure, however, changes dramatically during extended sliding; slip progressively localizes, thereby altering the drainage conditions. As the degree of localization, that is, the width of the deforming zone, significantly affects the degree of shear heating (Sibson, 1973), progressive localization and associated increased frictional heating can cause thermal pressurization if drainage is poor, so a perturbation of pore fluid pressure can persist. Slip localization appears to be affected by the effective normal stress on the fault. Low-velocity (0.1 μm/s–1 mm/s) friction experiments on saturated calcite gouges at a range of effective normal stresses show that comminution of particles after total displacements of <15 mm is much more pronounced at 50 MPa than at 1 MPa effective normal stress and that the development of discrete shear bands is only observed at the higher effective normal stress (Carpenter et al., 2016). Therefore, neither localization of slip nor significant shear heating and thermal pressurization are likely to occur at low effective normal stresses even for undrained conditions.

Here, we present the results of a suite of intermediate- to high-velocity (1 mm/s to 1 m/s) rotary-shear experiments on calcite gouges using a high-velocity friction apparatus with the capability of independently controlling normal stress and pore pressure. We complement the mechanical data by microstructural analysis to address the distinct, but interlinked objectives of establishing

1. the drainage conditions during shear to constrain the effective-stress coefficient α for (phases of) shear deformation;
2. the link between slip localization and effective normal stress and pore fluid pressure; and
3. the feedback of slip localization on shear strength.

Constraints on the evolution of drainage conditions in calcite gouges during shear paired with a quantification of the effective-stress behavior are important to judge the effects of the presence of fluids on the behavior of natural faults. Our work also provides the basis for evaluating the relative importance of thermal pressurization and potential switches in microdeformation mechanisms for dynamic weakening of calcite gouges.

2. Material and Methods

2.1. Experimental Setup and Procedure

Rotary-shear friction experiments were conducted with the *Phv*-apparatus at the Kochi Institute for Core Sample Research/JAMSTEC in Nankoku, Japan (Tadai et al., 2009; Tanikawa et al., 2012). The apparatus is equipped with a servo-controlled pore fluid pressure system (Rempe et al., 2017). During an experiment, the fluid pressure is servo-controlled using the upstream ($P_{f,up}$) fluid-pressure gauge located outside the sample holder. The axial load and displacement (i.e., the compaction or dilation of the sample in an axial direction) are monitored via a load cell and a displacement transducer, respectively (Figure 1a). Data are recorded at an acquisition rate of 1 kHz.

The gouge holder consists of an upper nonrotating part and a lower rotary part (Figure 1b). The sample chamber—lined with Teflon to reduce friction between the rotating and nonrotating parts—is annular with inner and outer diameters of 30 and 60 mm, respectively. The setup of fluid pressure inlet and outlet ensures that the pore fluid permeates the gouge material. The space between upper and lower parts of the holder is filled with pressurized fluid, thus reducing the normal load on the gouge layer and potentially affecting the measurement of the displacement transducers. A bypass tube between the fluid inlet and outlet ensures an equal fluid pressure upstream and downstream of the sample during an experiment. Nominally drained and undrained conditions were achieved by servo-controlling the fluid pressure and the fluid volume, respectively. The temperature evolution during an experiment is measured with two thermocouples that penetrate the nonrotating base plate and are thus in physical contact with the center of the ring-shaped gouge layer.

In the 35 experiments performed on room-dry and fluid-saturated calcite gouges, total displacements ranged from ~0.31 to 23 m (Table 1). We use an equivalent displacement, which accounts for the annular sample geometry as defined by Hirose and Shimamoto (2005). Only data for displacements less than ~4 m and microstructures from experiments with total displacements smaller than ~9 m were used for analysis, as for larger displacements gouges became contaminated with Teflon from the sample holder. During an experiment, up to two velocity steps were applied in direct succession using "subseismic" and "seismic" velocities of $v_1 = 1$ mm/s, and $v_2 = 1$ m/s, respectively. Velocity steps v_1 and v_2 are investigated separately from one another in the following. Some experiments were performed with velocity step v_1 (1 mm/s) or v_2 (1 m/s) only (Table 1). Normal stresses of 3 and 8.5 MPa were applied in experiments on dry gouges. In experiments on saturated gouges, the initial applied Terzaghi stress ranged from 0.5 to 11.2 MPa. To minimize fluid pressure buildup within the gouge layer, that is, to realize drained conditions, the bypass between upstream and downstream fluid pressure systems was open in most of the experiments (except in experiments Phv291 and 292, Table 1).

2.2. Sample Preparation and Microanalytical Techniques

The synthetic starting materials used in our experiments were derived from crushed Carrara marble, sieved to particle sizes <180 μm (Figure 1c). For each experiment, 15 g of gouge were put in the holder, yielding an initial precompacted gouge layer thickness of ~2.9 ± 0.2 mm. The gouge material was evenly distributed inside the gouge holder by turning the apparatus manually at a normal load of 1 kN. The gouge layer thickness was measured before each experiment using the position of the displacement transducer relative to that
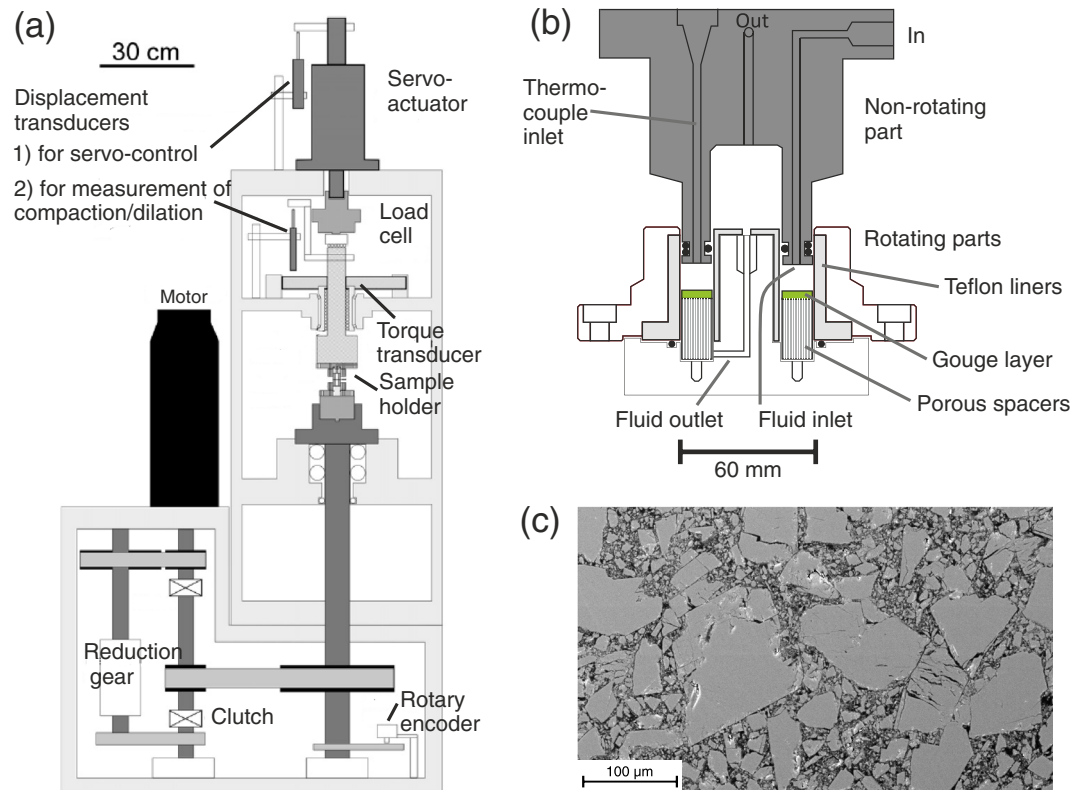
Figure 1. Experimental setup and starting material. (a) Schematic of the rotary shear apparatus *Phv* used in this study (modified from Tanikawa et al., 2012). (b) Sketch of the gouge holder (modified from Rempe et al., 2017). Fluid will pass through the tubes labeled In and Out, and through the sample chamber and the gouge layer that is marked in green and has an outer diameter of 60 mm. Gouge layer is not loaded in the sketch. (c) Backscattered electron image of the starting material, that is, unsheared Carrara marble gouge, precompacted at a normal stress of 0.15 MPa.

for an empty gouge holder (Figure 1a). In the saturated experiments, the gouge layer was presaturated by adding a few ml of distilled water to the gouge layer using a syringe and leaving it to saturate for ~1 hr before the axial pressure was applied. The sample was saturated by applying a servo-controlled fluid pressure of ≤1 MPa at the upstream pore fluid inlet while leaving the downstream vented to atmosphere. We use the data recorded during saturation to estimate the permeability of unsheared gouges at a normal stress of about 0.5 MPa employing Darcy's law. Once the water flow at the downstream was steady and free of air bubbles, the downstream end was closed and the downstream fluid pressure allowed to increase.

After an experiment, the preserved sample, most often recovered in one piece, was left to dry in air for at least 24 hr before it was impregnated with epoxy resin. The impregnated samples were cut normal to the sliding surface, and both parallel and perpendicular to the slip direction, to produce polished thin sections. Microstructural analysis was performed with scanning electron microscopy (SEM) for which the samples were coated with carbon or chrome. The SEM analysis was performed using a JEOL JSM-6500F Field-Emission SEM and a LEO (Zeiss) 1,530 Gemini high-resolution thermally aided Field Emission SEM. Images were taken in backscattered electron mode (BSE) with an acceleration voltage of 8–10 kV and a working distance of 7.5–10 mm.

2.3. Estimation of Permeability and Hydraulic Diffusivity

To evaluate the effect of the pore fluid pressure on mechanical data and microstructure evolution, we need to confirm that our experiments were performed under drained conditions. Assessing the drainage state of the gouges during the experiments requires the estimation of their hydraulic diffusivity (Wibberley, 2002),

Table 1
Experimental Conditions

	Exp. #	σ_T (MPa)	σ_n (MPa)	p_f (MPa)	$\lambda = p_f/\sigma_n$	Displ. (m) at $v_1 = 1$ mm/s	at $v_2 = 1$ m/s	Total	Accel. to v_2 (m/s²)	$\tau_{ss,v1}$ (MPa)	$\tau_{peak,v2}$ (MPa)	$\tau_{ss,v2}$ (MPa)
Water-saturated	phv305	0.51	2.0	1.5	0.75	0.31	17.8	18.11	0.5	0.42 ± 0.01	0.91 ± 0.01	0.37 ± 0.10
	phv290	0.69	7.7	7	0.91	0.4	21.2	21.60	0.5	0.60 ± 0.05	1.57 ± 0.03	0.72 ± 0.07
	phv337	0.69	7.7	7	0.91	0.31	4.55	4.86	0.5	0.62 ± 0.04	1.35 ± 0.00	0.57 ± 0.07
	phv346	0.69	7.7	7	0.91	0.31	—	0.31	—	0.59 ± 0.03	—	—
	phv347	0.69	7.7	7	0.91	—	3.88	3.88	0.5	— —	1.06 ± 0.07	1.65 ± 0.03
	phv354	0.69	7.7	7	0.91	—	6.16	6.16	0.1	— —	1.11 ± 0.01	0.29 ± 0.11
	phv355	0.69	7.7	7	0.91	0.31	1.87	2.18	0.5	0.58 ± 0.05	1.20 ± 0.01	0.28 ± 0.03
	phv306	0.93	1.1	0.2	0.15	0.31	18.6	18.91	0.5	0.79 ± 0.05	1.05 ± 0.02	0.54 ± 0.09
	phv351	1.04	11.5	10.5	0.91	0.3	3.73	4.03	0.5	0.83 ± 0.06	1.61 ± 0.00	0.48 ± 0.08
	phv340	2.02	8.0	6	0.75	0.3	4.62	4.92	0.5	1.47 ± 0.13	2.14 ± 0.01	0.90 ± 0.31
	phv304	2.50	4.0	1.5	0.38	0.31	18.5	18.81	0.5	2.03 ± 0.07	2.41 ± 0.01	1.09 ± 0.14
	phv310	2.80	3.4	0.6	0.18	0.31	5	5.31	0.5	2.21 ± 0.08	2.51 ± 0.01	1.04 ± 0.12
	phv313	2.80	3.4	0.6	0.18	—	5.32	5.32	0.5	— —	2.34 ± 0.01	1.28 ± 0.15
	phv338	2.80	3.4	0.6	0.18	—	6.08	6.08	0.1	— —	2.97 ± 0.01	1.26 ± 0.19
	phv342[a]	2.80	3.4	0.6	0.18	—	6.11	6.11	0.1	— —	2.45 ± 0.01	0.87 ± 0.13
	phv344	2.80	3.4	0.6	0.18	—	6.04	6.04	0.1	— —	2.29 ± 0.01	1.36 ± 0.19
	phv345	2.80	3.4	0.6	0.18	—	6.04	6.04	0.1	— —	2.50 ± 0.01	1.46 ± 0.23
	phv352	2.80	3.4	0.6	0.18	—	4.39	4.39	1	— —	2.79 ± 0.06	0.98 ± 0.21
	phv350	3.03	12.0	9	0.75	0.31	3.94	4.25	0.5	1.92 ± 0.21	2.45 ± 0.01	1.72 ± 0.38
	phv291[a]	8.01	9.5	1.5	0.16	0.4	21.9	22.30	0.5	5.94 ± 0.11	6.33 ± 0.00	2.56 ± 0.18
	phv292[a,b]	8.01	9.5	1.5	0.16	0.31	15.5	15.81	0.5	4.82 ± 0.10	5.20 ± 0.02	1.29 ± 0.19
	phv297[b]	8.01	9.5	1.5	0.16	0.31	18	18.31	0.5	5.60 ± 0.15	5.64 ± 0.01	1.92 ± 0.15
	phv298	8.01	9.5	1.5	0.16	0.31	17	17.31	0.5	5.86 ± 0.07	6.19 ± 0.01	2.19 ± 0.33
	phv300	8.01	9.5	1.5	0.16	0.31	9.6	9.91	0.5	5.86 ± 0.12	6.17 ± 0.01	2.95 ± 0.79
	phv312	8.01	9.5	1.5	0.16	0.31	4.81	5.12	0.5	5.64 ± 0.06	6.13 ± 0.01	1.87 ± 0.27
	phv307	9.34	11.3	2	0.18	0.31	4.2	4.51	0.5	6.47 ± 0.05	6.74 ± 0.01	2.08 ± 0.27
	phv309	11.21	13.6	2.4	0.18	0.31	12.2	12.51	0.5	8.15 ± 0.10	8.71 ± 0.01	2.06 ± 0.23
Dry	phv311	3.00	3	—	0	0.31	5.19	5.50	0.5	2.51 ± 0.24	2.63 ± 0.20	1.20 ± 0.09
	phv339	3.00	3	—	0	—	6.001	6.00	0.1	— —	2.90 ± 0.17	1.28 ± 0.38
	phv349	3.00	3	—	0	—	6.16	6.16	0.1	— —	2.86 ± 0.21	0.75 ± 0.18
	phv343	3.00	3	—	0	—	3.72	3.72	0.5	— —	2.79 ± 0.09	1.58 ± 0.10
	phv353	3.00	3	—	0	—	5.24	5.24	1	— —	2.78 ± 0.11	1.53 ± 0.19
	phv299	8.50	8.5	—	0	0.31	15	15.31	0.5	7.04 ± 0.15	7.99	1.70
	phv301	8.50	8.5	—	0	0.31	17	17.31	0.5	6.97 ± 0.17	8.16 ± 0.05	0.73 ± 0.17

[a] Bypass between upstream and downstream closed. [b] Volume-controlled (undrained) conditions. [c] For experiments in volume-control mode, initial values at the start of the experiment are given.

$$D_{\text{hyd}} = \frac{k}{\eta s}, \qquad (1)$$

where k is the permeability, s the specific storage capacity, and η the fluid viscosity. The specific storage capacity $s = \phi(c_{H_2O} + c_{pp})$ (Renner & Steeb, 2015) is a function of porosity ϕ, that we assume to be <40%, and the compressibility of the pore fluid, c_{H_2O}, and of the pore space, c_{pp}, the latter quantifying the dependence of the pore volume on pore fluid pressure. We neglect c_{pp} in the estimation of the variation of specific storage capacity, as (i) it is likely smaller than c_{H_2O} at room temperature (Wibberley, 2002) and hence does not affect s by much and (ii) to our knowledge no data exist on the dependence of c_{pp} on the relevant range in temperatures.

The permeability of unsheared and sheared gouges was measured using the steady-state flow method at essentially unloaded conditions (Terzaghi stresses of 0.5 MPa; unsheared) and a Terzaghi stress of 8 MPa, respectively (Table 2). Permeability perpendicular to slip direction of sheared gouges was determined for two samples that experienced 7 and 11 slip pulses, that is, acceleration to a slip velocity of 1 m/s followed by deceleration after a few m of slip, amounting to total displacements of ~80 m (phv295) and 13.5 m (phv296), respectively, and at a Terzaghi stress of 8 MPa. The pauses between the slip pulses allowed the gouge to cool preventing Teflon contamination due to its decomposition despite the relatively large displacements. A pore fluid pressure ≤0.7 MPa was applied upstream of the sample while the downstream end was

Table 2
Permeability Measurements

Sample	Displacement[a]	Normal stress (MPa)	Permeability (m^2)	±
phv346	unsheared	0.7	1.36E−16	9.60E−17
phv347	unsheared	0.65	1.51E−16	1.08E−16
phv355	unsheared	0.45	8.24E−17	5.83E−17
phv350	unsheared	0.4	1.49E−16	1.06E−16
phv295[b]	79.85 m	10	8.60E−17	6.90E−17
phv296[c]	13.43 m	10	2.15E−17	2.03E−17

[a]Reached in several slip pulses. [b]Measured after a displacement of 79.85 m at $v = 1$ m/s. [c]Measured after a displacement of 13.4 m at $v = 1$ m/s.

vented to atmospheric pressure. Once a steady-state flow was achieved indicating a constant fluid-pressure gradient $\Delta p_f = p_{up} - p_d$, permeability k was determined from the flow rate Q employing Darcy's law, $k = Q\eta L/\Delta p_f A$, where A is the cross-sectional area of the sample and L the sample thickness.

For unsheared gouges, the permeability ranges between $6 \cdot 10^{-17}$ and $1 \cdot 10^{-16}$ m^2. Although the difference in displacements of the two tested sheared gouge samples was relatively large (13.5 and 80 m), they exhibit similar permeabilities of $9 \cdot 10^{-17}$ and $2 \cdot 10^{-17}$ m^2, respectively, suggesting that the difference to the displacements in our main experiments (Table 1) does not significantly affect permeability. Comparison to literature results and considering the relatively large displacements that our gouges experienced suggest that the results of our permeability measurements likely provide a lower bound for the permeability and thus, hydraulic diffusivity, of our sheared gouges. Similar permeability values were previously determined for water-saturated carbonate gouge sheared at 10 µm/s at a Terzaghi stress of 3–10 MPa following a displacement of 2.5 cm ($5 \cdot 10^{-17}$ to $7 \cdot 10^{-18}$ m^2, Scuderi & Collettini, 2016). Significantly higher permeability values were obtained by measurements using nitrogen gas on carbonate gouges sheared at 1.2 m/s at 2 MPa after a shear displacement of 14–17 m ($2 \cdot 10^{-14}$ m^2 at 2–3 MPa) (Han et al., 2010), and in gouge material produced by shearing intact carbonate rocks ($1 \cdot 10^{-15}$ m^2 at 2 MPa) (Delle Piane et al., 2016).

Hydraulic diffusivity will change during shear not only due to a change in microstructural state of the gouge, affecting its porosity and permeability but also due to the temperature-dependence of viscosity η and compressibility c_{H_2O} of pore water (Figures 2a and 2b). This effect of shear heating on η and c_{H_2O} for a constant microstructural state yields a gradual increase in D_{hyd} for liquid water with increasing temperature by ~1 order of magnitude, followed by a sudden drop in D_{hyd} by about 2 orders of magnitude upon vaporization of the pore water (Figure 2c), caused in particular by the compressibility increase by 3 to 4 orders of magnitude (Figure 2b). Following vaporization, viscosity, compressibility, and hydraulic diffusivity are approximately constant up to 600°C. The decreases in permeability and porosity counterbalance each other to some degree in their effect on hydraulic diffusivity (Equation 1; Figure 2c).

Relying on the standard scaling relation between the characteristic length scale of a diffusion process and its characteristic time, $D_{hyd} \sim l_{char}^2/t_{char}$, we estimate the time needed to achieve drained conditions for the on-average 2.9-mm-thick gouge layers to be ~0.01 s at room temperature, independent of fluid pressure (Figure 2d). The characteristic time increases to 0.4–1.5 s when shear heating causes the pore water to vaporize. The drainage state can be evaluated by comparing the characteristic time to the duration of different deformation phases during the experiment.

3. Results

3.1. Mechanical Data

For the sake of clarity of figures, we will first present our mechanical data as a function of Terzaghi stress, that is, assuming that the effective-stress coefficient $\alpha = 1$. As we will show later (in section 4.3), the effective-stress coefficient for frictional strength of carbonate gouges is indeed very close to unity, which means that for our experiments $\sigma_{eff} = \sigma_T$. Furthermore, we use a representative subset of our data obtained at Terzaghi stresses of 8–8.5 MPa to describe the evolution of shear stress, apparent friction coefficient, axial displacement, temperature, and fluid pressure during shearing at the two imposed velocities. The apparent coefficient of friction, $\mu_{app} = \tau/\sigma_T$, is "apparent" because it is calculated from the Terzaghi stress σ_T as surrogate for the unknown true effective normal stress σ_{eff}. Subsequently, we will report the effect of the Terzaghi stress on the shearing behavior.

3.1.1. Subseismic Slip Rates (1 mm/s)

Dry gouges sheared at 1 mm/s and a normal stress of 8.5 MPa reach a peak shear stress of ~7 MPa, corresponding to coefficient of friction of 0.82 (Figures 3a and 3b). The shear stress remains constant over the total displacement of ~30 cm. In the presence of pressurized fluids—but for nominally almost identical Terzaghi
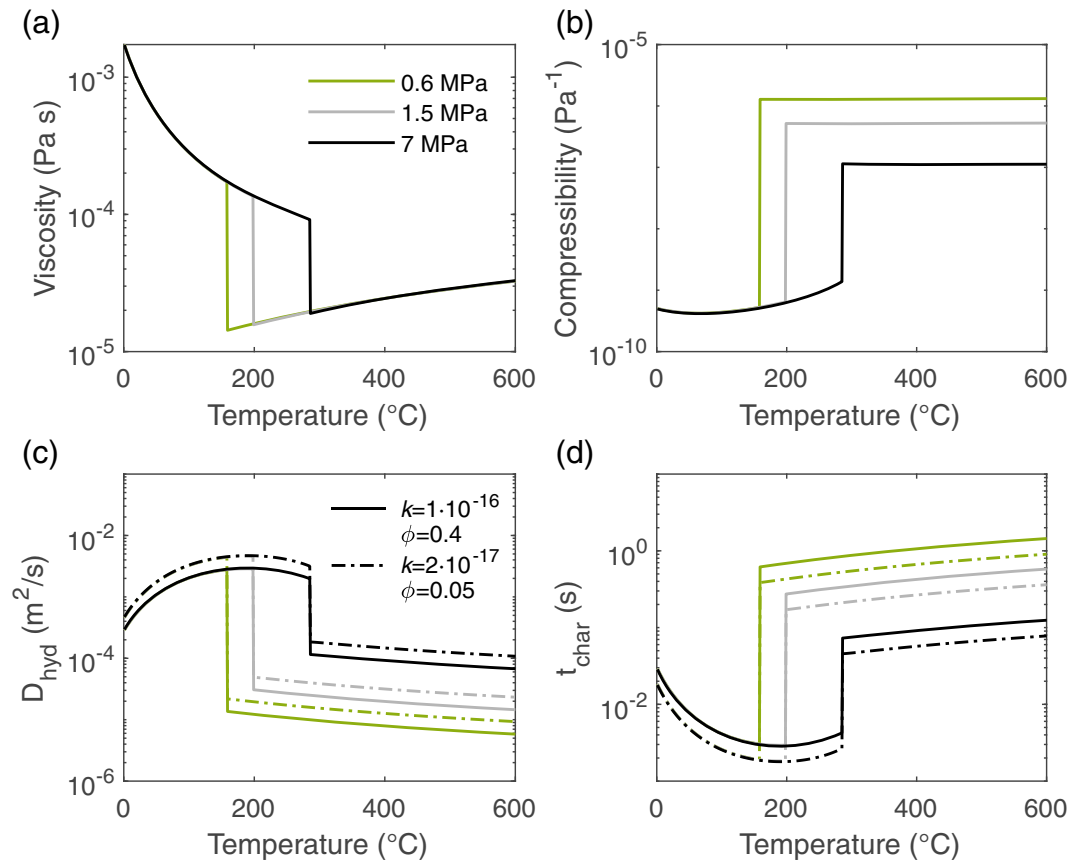
Figure 2. Viscosity, compressibility, hydraulic diffusivity and characteristic time as a function of temperature. (a) Viscosity η, (b) compressibility c_{H_2O}, (c) hydraulic diffusivity $D_{hyd} = k/(\eta c_{H_2O}\phi)$, and (d) characteristic time $t_{char} = l_{char}^2/D_{hyd}$ as a function of temperature for fluid pressures of 0.6, 1.5, and 7 MPa. While viscosity of water decreases by approximately 2 orders of magnitude upon heating and vaporization, its compressibility is approximately constant until vaporization induces a compressibility increase by 3 to 4 orders of magnitude. The hydraulic diffusivity was calculated for two different combinations of permeability k (in m^2) and porosity ϕ (see legend) and neglecting the contribution of the pore space compressibility (see main text). The temperature dependence of viscosity and compressibility causes an increase of the hydraulic diffusivity of liquid water by about 1 order of magnitude upon heating and a sudden drop by ~2 orders of magnitude upon vaporization, yielding a sudden increase in the characteristic time upon vaporization as well. Data were calculated with the software FLUIDCAL (Wagner, 2009) based on equations of state by Sengers and Kamgar-Parsi (1984) and Wagner and Pruß (2002).

stress conditions—the "steady-state" shear stress and corresponding apparent coefficient of friction of ~0.71–0.74 are lower than for dry conditions, and slight slip-weakening behavior is observed (Figures 3a and 3b).

The presence of pressurized water enhances compaction during the low-velocity shearing (Figure 3c). Dry gouges compact only at the initiation of shearing, while compaction continues throughout the displacement of 30 cm in the saturated samples. Over the 30 cm of displacement, the temperature increases only moderately, by ~10°C for dry and 8°C for saturated gouges (Figure 3d). This increase in temperature is too low to induce a significant degree of thermal pressurization of the pore fluids. In the two fluid-volume controlled experiments, the downstream fluid pressure increases by only 0.2–1.2 MPa (Figure 3e), which is likely caused by the shear-induced compaction of the gouge rather than the modest temperature increase. The increase in fluid pressure in the two experiments is responsible for the slightly larger decrease in shear stress observed after a few mm to cm of slip in the fluid volume-controlled experiments compared to the pressure-controlled experiments (Figure 3a), as an apparent coefficient of friction of 0.73–0.79 is maintained in all experiments with saturated gouges (Figure 3b).
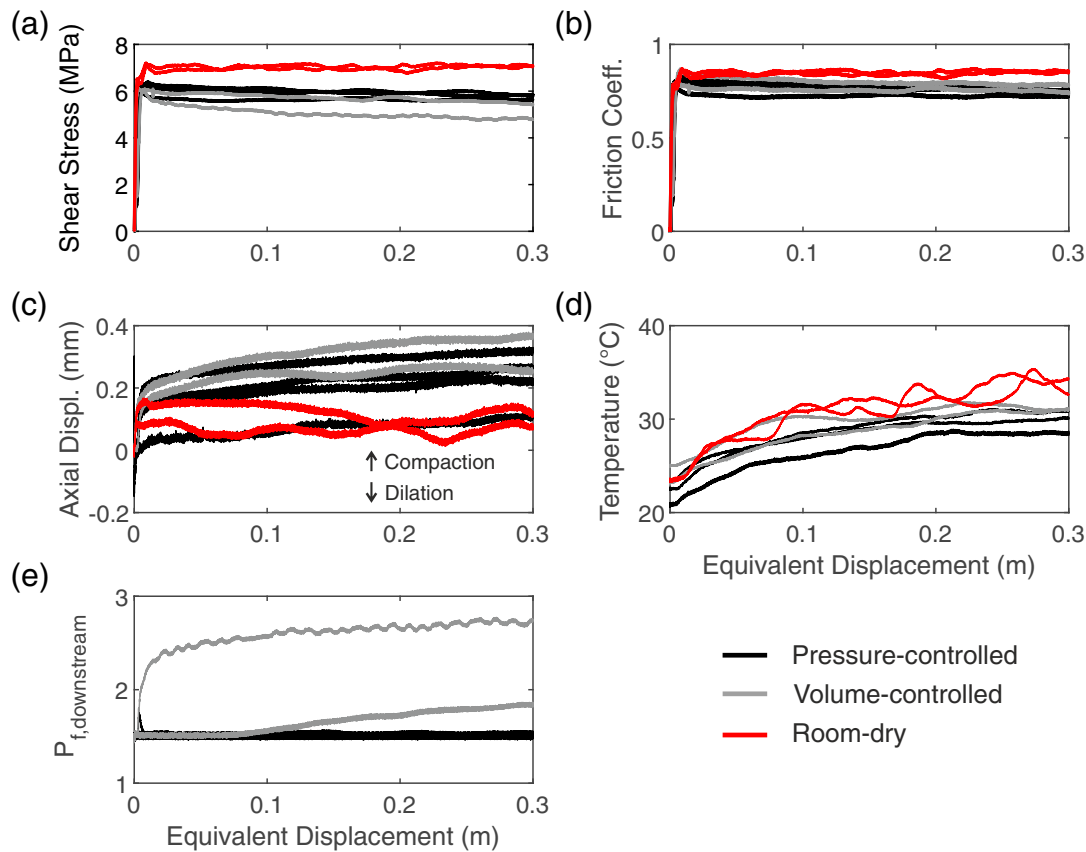
Figure 3. Experimental records as a function of displacement conducted at low velocity (1 mm/s) a Terzaghi stress of 8–8.5 MPa. (a) Shear stress; (b) apparent coefficient of friction; (c) axial displacement, where a positive change denotes compaction; (d) temperature of the gouge layer; and (e) downstream pore fluid pressure.

3.1.2. Seismic Slip Rates (1 m/s)

The behavior at the initiation of sliding is quite different for dry and saturated samples at the high slip rate. At the initiation of sliding at high velocity (1 m/s), the dry gouges strengthen to a peak shear stress of ~8 MPa (corresponding to an apparent peak coefficient of friction $\mu_{peak} \approx 0.94$) within the first 20 cm of slip (Figures 4a–4d). Subsequently, the shear stress decreases to a steady-state value of $\tau_{ss} \approx 2$ MPa. The peak shear stress of the saturated gouges is lower than that of the dry gouges, ranging from 5 to 6 MPa ($\mu_{peak} \approx 0.6$–0.75). Dynamic weakening of saturated gouges initiates immediately following initiation of acceleration to 1 m/s, that is, they do not show a clear strengthening phase (Figures 4a and 4b). Shear stress and apparent friction coefficient during the steady-state phase are slightly higher in dry gouges than in water-saturated gouges (Figures 4a–4d).

The degree of compaction is higher in dry gouges (up to almost 400 μm during a shear displacement of 4 m, Figure 4e) than in saturated gouges, which even show transient dilation after c. 40 cm of shear displacement (Figure 4f). The dilation is most pronounced in volume-controlled (undrained) conditions and continues after a minor amount of compaction, while transient dilation in pressure-controlled (nominally drained) conditions is followed by continued compaction, albeit by only 100 μm (Figure 4e). The temperature increases significantly throughout the high-velocity step, reaching ~150°C to 550°C at 4 m of total displacement (Figures 4g and 4h). In general, the temperature increase is smallest in volume-controlled (undrained) experiments, but relatively similar for dry and pressure-controlled (drained) conditions. Fluid-pressure increases by ~2–3 MPa in the volume-controlled experiments (Figures 4i and 4j). In contrast to the low-velocity step (Figure 3a), this increase in fluid-pressure does not seem to result in a corresponding decrease in the shear stress, that is, the shear stress is similar in pressure- and volume-controlled experiments (Figure 4a). Because this fluid-pressure increase occurs as the sample dilates (Figures 4e and 4i; rather than compacts like for the low-velocity step, Figure 3c), the pressurization as well as the dilation are likely
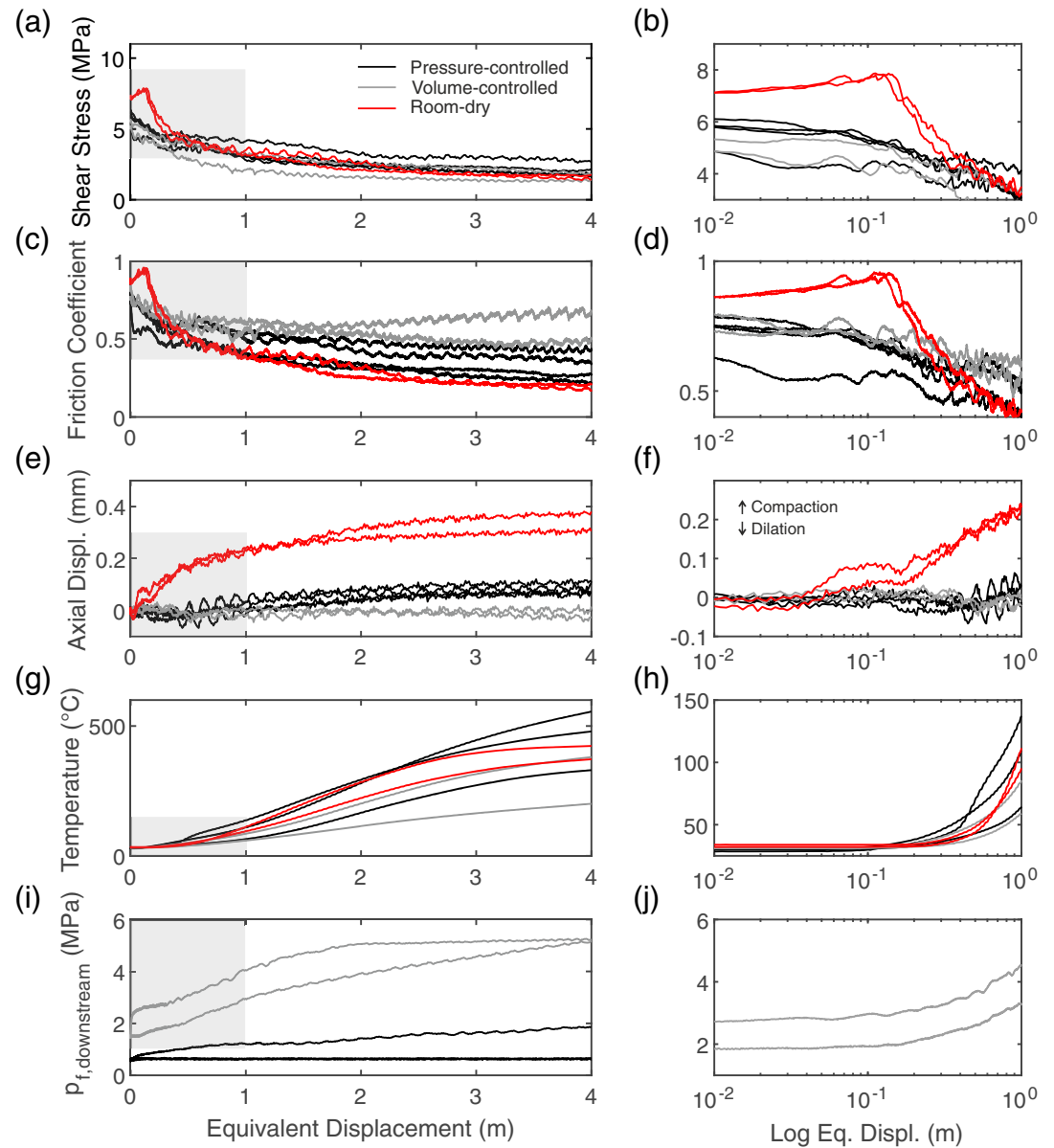
Figure 4. Experimental records as a function of displacement conducted at high velocity (1 m/s) and a Terzaghi stress of 8 to 8.5 MPa. (a, b) Shear stress; (c, d) apparent friction coefficient; (e, f) axial displacement, where a positive change denotes compaction; (g, h) temperature of the gouge layer; and (i, j) downstream pore fluid pressure. In (i), the increase in pore pressure for one pressure-controlled experiment is due to the closed bypass between upstream and downstream fluid pressure system (phv291). The increase in fluid pressure in the volume-controlled experiments is accounted for in the calculation of the friction coefficient. Shaded areas in the plots on the left represent the sections presented on the right using a logarithmic scale to show the behavior at the initiation of slip at high velocity.

due to the significant temperature increase. The apparent friction coefficient in volume-controlled experiments, corrected for the fluid-pressure increase assuming $\alpha = 1$, is relatively high in comparison to the pressure-controlled experiments (0.5–0.7 compared to 0.23–0.45, Figure 4c). This relatively high apparent friction coefficient is likely due to the Terzaghi stress decreasing as the fluid pressure increases. We further investigate this effect of Terzaghi stress on frictional strength in the following section.

3.1.3. Effect of Terzaghi Stress on Mechanical Behavior

Shear stress of saturated gouges sheared at 1 mm/s and 1 m/s increases systematically with increasing Terzaghi stress, while the apparent coefficient of friction decreases (Figures 5a–5d). For fluid-saturated conditions and a Terzaghi stress of 8 MPa, the steady-state shear stress at a sliding velocity of 1 mm/s is on the
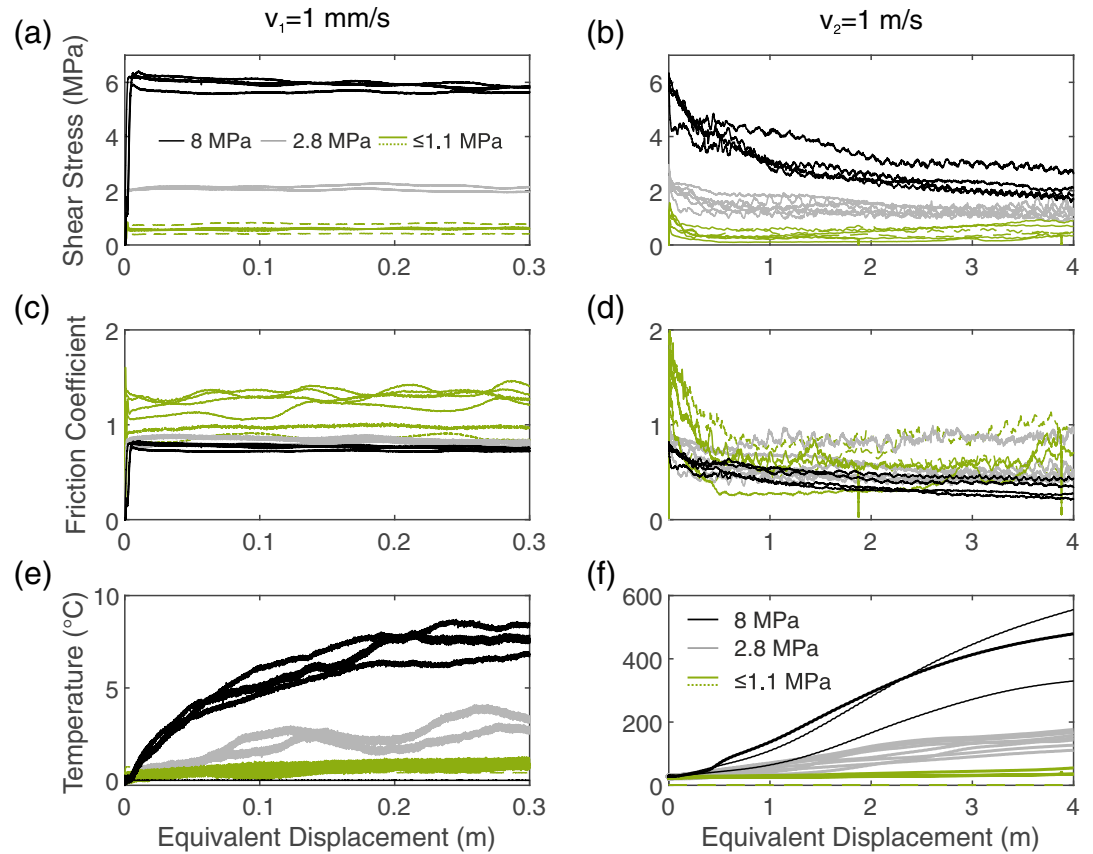
Figure 5. The effect of Terzaghi stress on the mechanical and temperature data for fluid-saturated experiments. (left column) Low-velocity step (1 mm/s), (right column) high-velocity step (1 m/s). (a, b) Shear stress. Full and dashed green lines denote experiments performed at low Terzaghi stress realized using high (7 MPa) and low pore fluid pressures (0.2 to 1.5 MPa), respectively; the pore fluid pressure does not appear to affect the mechanical behavior significantly. (c, d) Apparent friction coefficient, (e, f) temperature, where (e) shows the increase in temperature relative to the temperature at the start of the experiment while (f) shows the absolute temperature.

order of 5.6–5.9 MPa ($\mu_{\text{ss,slow}} = 0.71$–$0.74$). In contrast, it only reaches 2.2 MPa ($\mu_{\text{ss,slow}} = 0.79$) for a Terzaghi stress of 2.8 MPa, and is even reduced to ~0.6 MPa ($\mu_{\text{ss,slow}} = 0.81$–$0.9$) for fluid-saturated gouges sheared at Terzaghi stresses of 0.7–1.1 MPa (Figure 5a). During the high-velocity stage, the shear stress of fluid-saturated gouges reaches peak values of 6.1–6.3 MPa ($\mu_{\text{peak}} = 0.77$–0.79), 2.3–2.8 MPa ($\mu_{\text{peak}} = 0.82$–1.0), and 1–1.6 MPa ($\mu_{\text{peak}} = 1.5$–2.3) for Terzaghi stresses of 8, 2.8, and 0.7 MPa, respectively (Figure 5b). The data show a dependence of shear stress and—apparently—friction coefficient on Terzaghi stress, that is well addressed by the Coulomb law

$$\tau = \mu \sigma_{\text{T}} + c, \tag{2}$$

as it accounts for cohesion c. For dry as well as fluid-saturated gouges, shear stress τ depends on the Terzaghi stress σ_{T} in a linear fashion (Figure 6), yielding apparent friction coefficients $\mu_{\text{dry}} = 0.82 \pm 0.05$ and $\mu_{\text{sat}} = 0.69 \pm 0.002$ for the steady-state shear stress during the low-velocity step (Figure 6a) and $\mu_{\text{dry}} = 0.98 \pm 0.014$ and $\mu_{\text{sat}} = 0.68 \pm 0.0004$ for the peak shear stress at high velocity (Figure 6b). The steady-state shear stress measured during the high-velocity step shows no or a relatively small dependence on Terzaghi stress for dry and saturated conditions, respectively ($\mu_{\text{dry}} = -0.03 \pm 0.03$ and $\mu_{\text{sat}} = 0.18 \pm 0.01$, respectively; Figure 6b).

The temperature increase during sliding is significantly larger, the higher the Terzaghi stress. At a Terzaghi stress of 0.7 MPa, the temperature increase is negligible at both low and high sliding velocity (Figures 5e and 5f), while at a Terzaghi stress of ~3.0 MPa and higher, the temperature increase is significant (100–550°C, Figure 5f) for both dry and saturated gouges sheared at 1 m/s. The pore fluid pressure remains
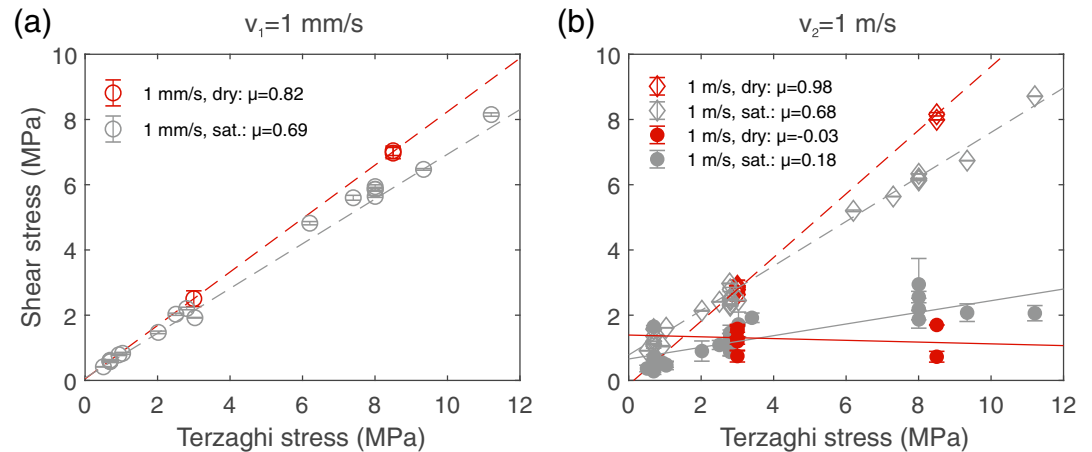
Figure 6. Dependence of shear stress on Terzaghi stress for (a) low-velocity and (b) high-velocity phase. (a) Shear stress at steady-state conditions from low-velocity step and (b) peak shear stress from high-velocity step (open symbols) show clear dependence on Terzaghi stress. Steady state shear stress at high velocity (subplot b, full symbols) shows no dependence on normal stress for dry conditions and a negligible dependence for saturated conditions. Lines mark best fit to data using Equation 2, such that slope corresponds to the coefficient of friction μ as given in legend. Error bars are mostly smaller than symbol size.

nominally constant in most experiments (Figures 3e and 4i) and—beyond its contribution to Terzaghi stress—its absolute value does not seem to play a distinct role for shear stress, axial displacement, or temperature evolution.

3.2. Microstructures

Below we report the results from microstructural analysis conducted on gouge layers sheared for 5–6 m at a velocity of 1 m/s. While dry samples were only preserved after experiments conducted at Terzaghi stresses of 3 MPa, we present microstructural data for the whole range of applied Terzaghi stresses for saturated samples.

All dry samples sheared at a normal stress of 3 MPa and at high velocity show comparable microstructures (Figure 7). The sheared gouge layers exhibit three distinct textural zones (as previously described by Rempe et al., 2014), which compare to the starting material (Figure 1c) as follows: (1) a zone with relatively unaltered microstructural features, that is, with relatively large particle size and high porosity (Figure 7a); (2) a zone, in which few relict clasts are dispersed in a matrix of relatively smaller particles, apparently the product of comminution (Figures 7a and 7b); and (3) an ~15–20 μm thick zone flanking the localized principal slip surface, composed by aggregates of apparently recrystallized, elongate calcite grains (Figures 7c and 7d). This principal slip surface always developed close to the upper, nonrotating side of the gouge holder (see Beeler et al., 1996). The recrystallites in Zone 3 are micrometer to submicrometer in size and their long axes are oriented ~15–20° to the principal slip surface, consistent with the dextral sense of shear (Figure 7d). The degree of recrystallization decreases toward textural Zone 2 and the porosity increases. Degassing channels provide evidence for decarbonation, indicating that temperatures in Zone 3 locally exceeded the measured temperatures (Figure 7d) (Violay et al., 2013).

Gouges sheared in the presence of pressurized water at Terzaghi stresses of 2.8–3 MPa also have three textural zones (Figure 8) similar to those observed in the dry samples (Figure 7). However, sample-to-sample variability is higher than for the dry samples. For instance, in sample phv344 (Figures 8a–8c), some fragments of reworked material from Zone 3 in textural Zone 2 (Figure 8b) show sintered grains and degassing channels along the principal slip surface (Figure 8c). Textural Zone 3 of sample phv313, on the other hand, is characterized by recrystallized grains in a ~10-μm-thick zone along the principal slip surface (Figures 8d–8f). In sample phv350 recovered after an experiment performed at a Terzaghi stress of 3 MPa and a relatively high pore fluid pressure of 9 MPa, textural Zones 1 and 2 both have a relatively low porosity and are distinguishable from each other due to differing grain sizes (Figure 8g). Textural Zone 2 exhibits several Riedel shears and boundary (Y-)shears (Figure 8h) along which grain size reduction is intense (possibly corresponding to textural Zone 3; Figure 8i). As no recrystallization or sintered material was observed, the
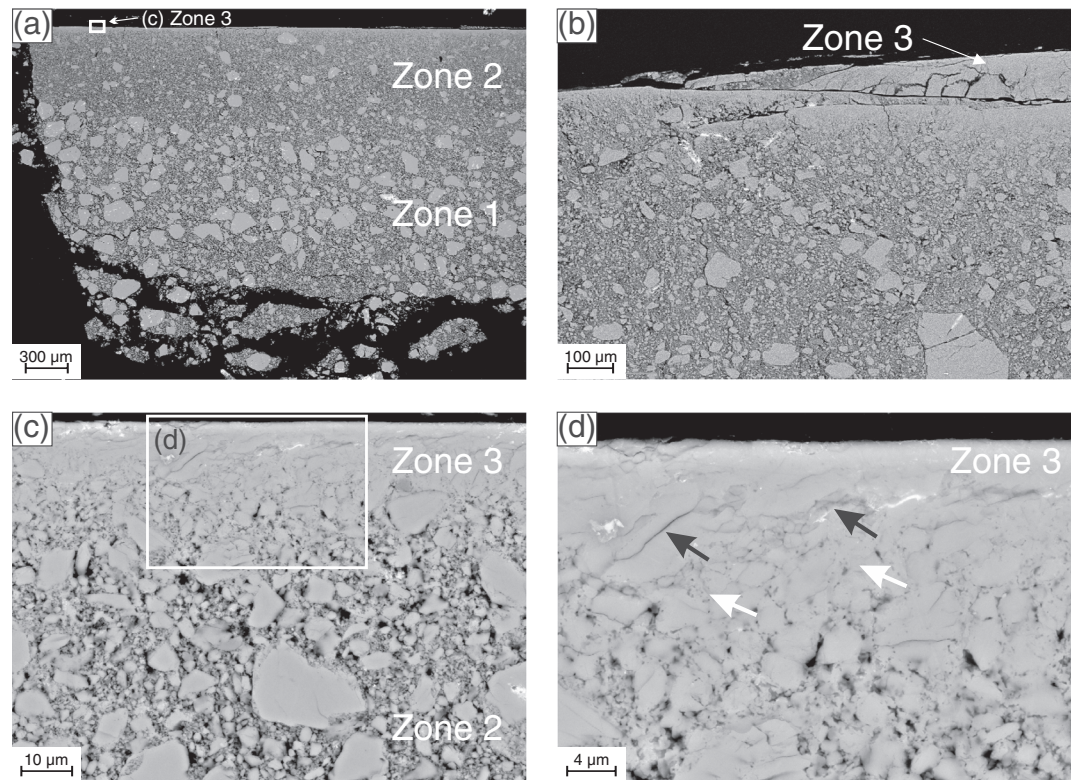
Figure 7. Microstructures of dry gouges sheared at high velocity (1 m/s) to a total displacement ≤6 m at a Terzaghi stress of 3 MPa. (a) Development of three distinct microstructural zones (sample phv353). (b) Multiple slip surfaces developed during the course of the experiment (sample phv339). (c) Zoom of area marked by arrow and rectangle in (a), and (d) zoom of area marked in (c), showing that intense localization leads to sintering of grains, which exhibit a preferred orientation (black arrows). Degassing channels marked by white arrows in (d) provide evidence of decarbonation. The shear sense is dextral in all images.

deformation of this sample sheared at a pore fluid pressure of 9 MPa appears to be less intense compared to that in samples phv344 and phv313 (pore fluid pressure of 0.6 MPa; Figures 8a–8f).

Samples sheared at 1 m/s to displacements of 5–6 m at a Terzaghi stress of 8 MPa exhibit three textural zones (Figure 9) similar to those found in the gouge layers sheared at ~3 MPa (Figures 7 and 8). However, these textural Zones 2 and 3, characterized by intense grain size reduction and sintering of grains, respectively (Figure 9c), are wider compared to the textural zones from the samples sheared at lower Terzaghi stress.

Microstructures from samples deformed at low Terzaghi stress of 0.7 MPa (Figure 10) have a significantly different appearance compared to those sheared at higher stress. Imprints of the roughness of the gouge-holder base plates in the samples evidence that the bulk of the gouge layer was preserved during sample preparation (Figures 10a and 10b). Distinct textural zones are not developed (Figures 10a and 10b). In gouges sheared at low velocity (1 mm/s) for a short total displacement of 0.31 m, porosity varies modestly throughout the gouge layer (Figure 10a). Incipient shear bands are recognized in samples sheared at 1 m/s for ~6 m (Figures 10b and 10c), but a textural zone 3 (i.e., a smooth principal slip surface bounded by recrystallized or sintered calcite grains) did not develop during shear. In summary, this type of microstructure differs significantly from the microstructure developed at higher Terzaghi stress. Therefore, within the range tested, the Terzaghi stress appears to have a significant effect on degree of comminution and localization.

4. Discussion

Potential weakening mechanisms induced by high slip rates or the presence of fluids in calcite gouges as well as cohesive carbonate rocks have been the subject of a number of previous studies (Chen et al., 2017; Han, Shimamoto, Ando, & Ree, 2007; Han, Shimamoto, Hirose, et al., 2007; Han et al., 2010; Mitchell et al., 2015;
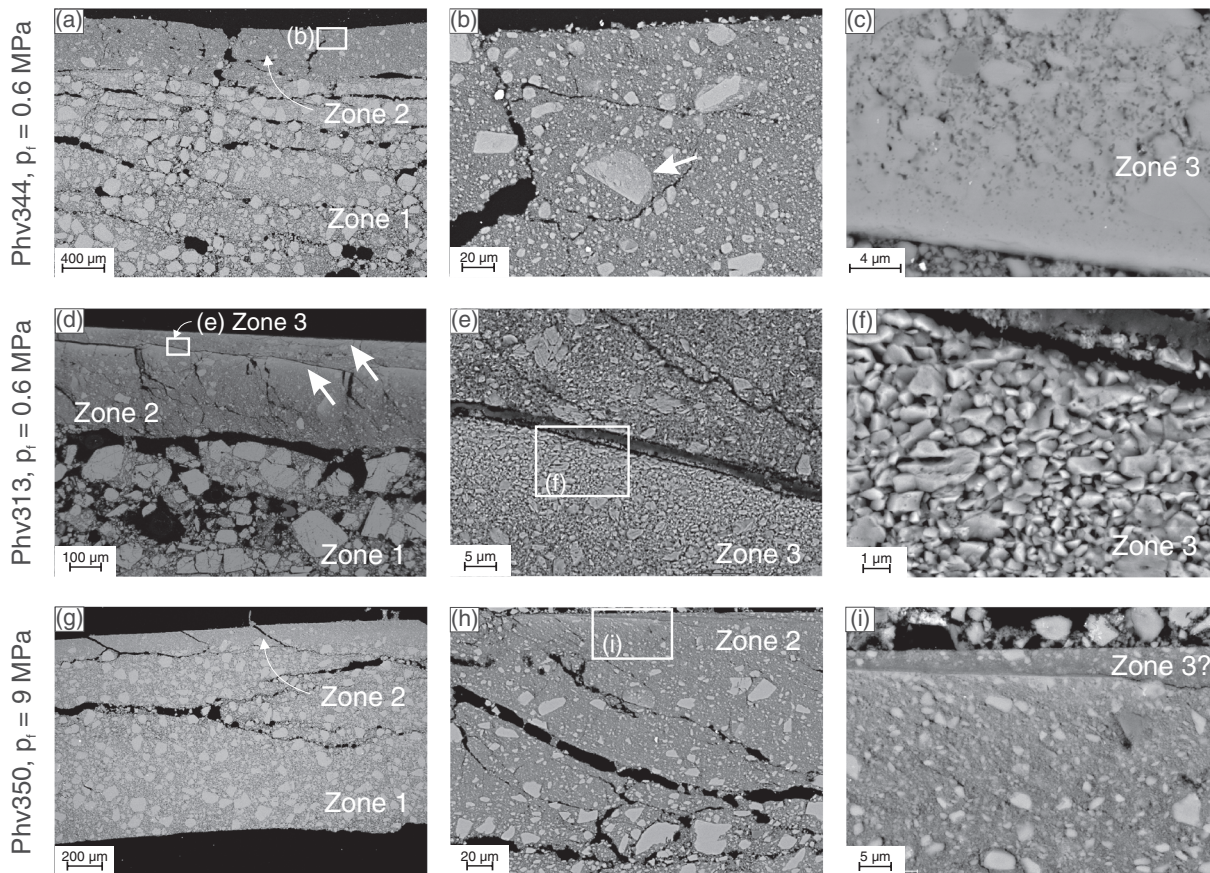
Figure 8. Microstructures of water-saturated gouges sheared at high velocity (1 m/s) and a Terzaghi stress of ~3 MPa to a total displacement ≤6 m. (a–c) Sample phv344, which exhibits characteristics similar to the dry samples. (a) Two distinct microstructure zones are distinguishable. (b) Within Zone 2, fragments of the slip surface (white arrow) can be found. (c) A fragment of the PSS showing degassing channels and sintered grains. (d–f) Sample phv313, deformed under the same conditions as phv344, shows three textural zones and a primary and a secondary principal slip surface (arrows). (e and f) Within a zone along the PSSs a few tens of μm in thickness, grains are recrystallized. (g–i) Sample phv350, sheared at a Terzaghi stress of 3 MPa, but higher pore fluid pressure (9 MPa) than phv344 and phv313 exhibits two distinguishable textural zones and low porosity. A principal slip zone (textural Zone 3) may be developing (i).

Rempe et al., 2017; Smith et al., 2015; Verberne, Plümper, et al., 2014; Violay et al., 2013, 2015; Yao et al., 2018). Therefore, we will focus the discussion on the following unresolved key questions:

1. What are the drainage conditions of the experimental gouge layers during intermediate- (1 mm/s) and high- (1 m/s) velocity sliding, that is, are the mechanical and microstructural data potentially affected by undetected elevated pore pressure due to undrained conditions?
2. What are the parameters of the effective-stress law for the shear strength of calcite gouges deformed at intermediate to high sliding velocity?
3. Do the pore fluid pressure and, in particular, thermal pressurization affect the frictional strength of calcite gouges and their dynamic-weakening process?
4. How is the microstructural development of calcite gouges, specifically the degree of slip localization as a major control of frictional heating, influenced by effective normal stress during intermediate- to high-velocity sliding?

4.1. Evaluation of Drainage Conditions During Shear

The short characteristic time for diffusion (~0.01 s at room temperature; Figure 2d) implies that conditions were drained throughout the low-velocity stage of the experiments (1 mm/s), where reaching quasi steady-state behavior required tens of seconds after the initiation of sliding (Figure 3a) and shear heating is insignificant. In the high-velocity stage, fluid-saturated gouges start to weaken dynamically as soon as sliding at 1 m/s initiates, namely at slip displacements <0.01 m (Figures 4a and 4b). To reach these displacements requires times on the order of 0.1–0.3 s, considering the applied accelerations (0.1–1 m/s^2; Table 1),
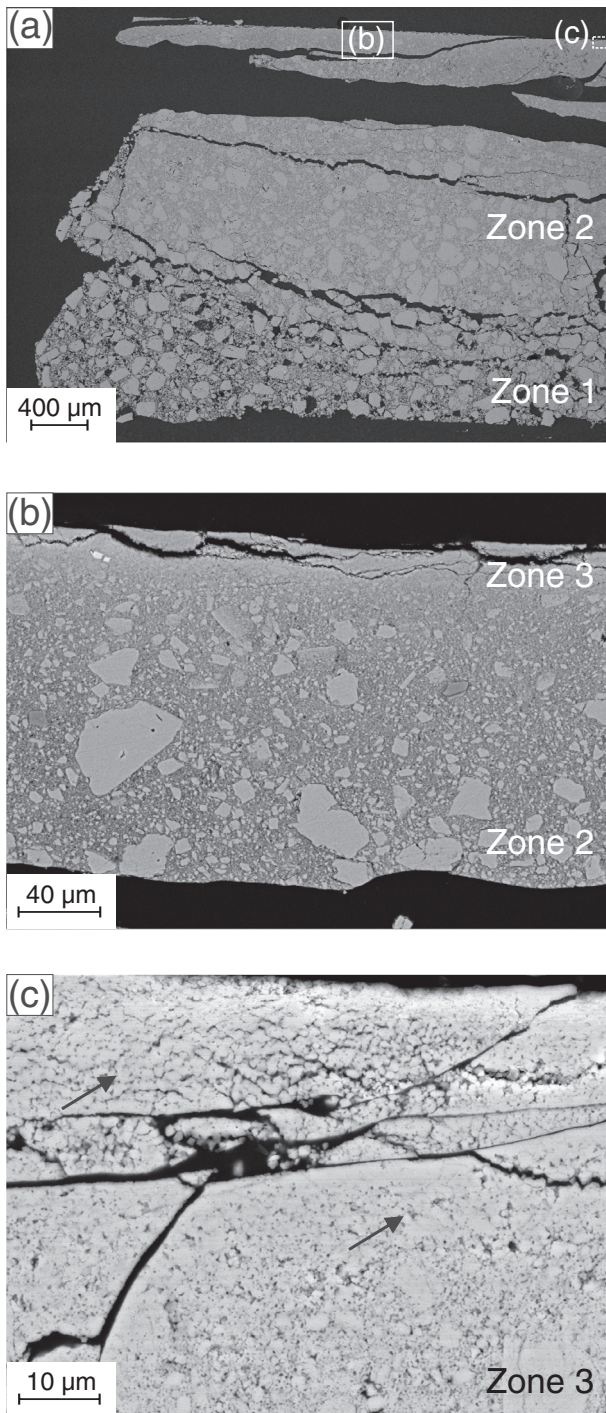
Figure 9. Microstructures of water-saturated gouges sheared at a Terzaghi stress of 8 MPa (sample phv312). (a) Cross section through whole sample clearly showing the three textural zones: a high-strain, an intermediate-strain, and a low-strain zone, marked by the decrease in degree of comminution/increase in size of particles. (b and c) Zooms of zones marked with white rectangles in (a): The zone adjacent to the principal slip surface is characterized by intense grain size and porosity reduction, sintering of material, and potentially incipient recrystallization (regions marked by arrows). Abundant small holes in (c) give evidence of decarbonation.

which are longer than the characteristic diffusion times. Fluid-pressure transients caused by the abrupt accelerations will therefore have had time to equilibrate within the fluid system before dynamic weakening initiates. Thus, conditions are likely fully drained at this point and dynamic weakening is unlikely influenced by elevated pore pressures.

The further evolution of drainage conditions during the high-velocity step depend on the applied Terzaghi stress as it controls the degree of frictional heating and the properties of the pore fluid. Following dynamic weakening during high-velocity steps on fluid-saturated gouges, temperatures reach ~50°C and 100–170°C for Terzaghi normal stresses of 1 and 2.8 MPa, respectively, and up to 550°C at a Terzaghi stress of 8 MPa. Locally, temperatures might be higher than these values measured at the gouge layer/base plate interface, but we expect that measured temperatures are representative for the bulk gouge material because the tips of the thermocouples are in contact with the surface of the gouge layer where localization occurs. At face value, for experiments at a Terzaghi stress of 1 MPa, temperatures were below those required for pore water vaporization regardless of the fluid pressure, resulting in short characteristic times ($t_{char} < 0.008$ s) and drained conditions. The fluid pressure in the majority of experiments conducted at $\sigma_T = 2.8$ MPa was 0.6 MPa; in these, recorded temperatures exceeded the vaporization temperature (~158°C; Figure 2) after a displacement of 1.7–3.4 m (Figure 5f). Thus, characteristic times were smaller than 0.03 s in the early stages of slip, while reaching ~0.7 s at the larger displacements. Similarly, for the experiments conducted at $\sigma_T = 8$ and $p_f = 1.5$ MPa, recorded temperature exceeded the vaporization temperature (200°C; Figure 2) and characteristic times were on the order of 0.5 s. As these characteristic times for experiments at $\sigma_T = 2.8$ and $\sigma_T = 8$ MPa are only 1 order of magnitude shorter than the duration of the experiments (i.e., seconds), poor drainage might affect the high-velocity, "steady-state" mechanical data at Terzaghi stresses of 2.8–8 MPa. Since axial displacement and temperature records differ for volume-controlled and pressure-controlled experiments at 8 MPa, conditions were at least partially drained during our pressure-controlled experiments; otherwise, the data should be identical to those from volume-controlled experiments, as these correspond to externally undrained conditions. For natural fault zones, it was previously suggested that permeability is created during earthquake slip (Sibson, 1992), improving drainage of pressurized fluids from the slipping zone. Therefore, it might be concluded that drained conditions are likely achieved during seismic slip velocities >1 m/s. However, as characteristic diffusion times depend not only on permeability and porosity but also on temperature and pressure conditions (Figure 2), ultimately, drainage conditions might vary for natural fault zones.

4.2. Effective-Stress Dependence of Shear Stress

Since drained conditions prevail during the low-velocity steps and we independently measured shear stress, normal stress, and pore pressure, our experimental data allow us to derive an effective-stress law for the shear strength of calcite gouges sheared at low velocity,

$$\tau = \mu\sigma_{eff} + c = \mu(\sigma_n - \alpha p_f) + c, \qquad (3)$$

where the constant c represents cohesion. Contrary to the Coulomb law of Equation 2 and to the presentation of data as a function of Terzaghi stress
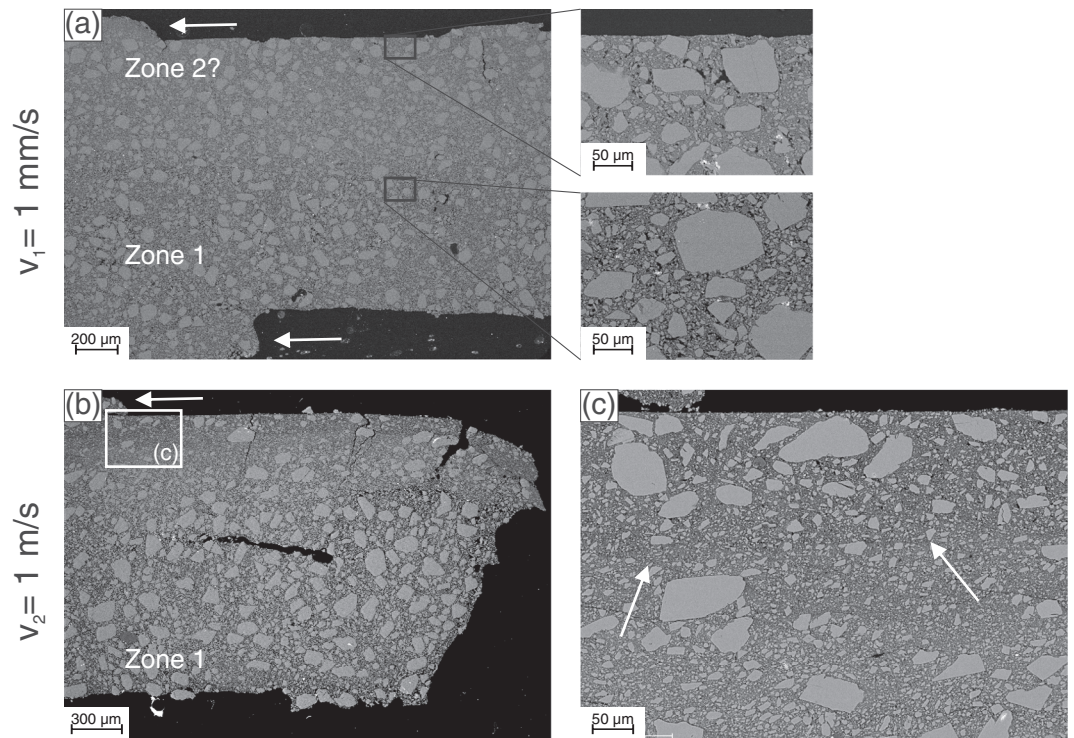
Figure 10. Microstructures of fluid-saturated gouges sheared at a Terzaghi stress of 0.7 MPa. (a) Sample phv346 sheared only at low velocity (1 mm/s) for a total displacement of 31 cm. Deformation is distributed relatively homogeneously across the gouge layer, but the porosity is slightly reduced close to the side of the gouge layer where the PSS typically develops (upper zoom) compared to the center of the gouge layer (lower zoom), potentially documenting an incipient textural Zone 2. Imprints from the roughness of the gouge holder base plates can be seen at both upper and lower boundaries of the gouge layer (white arrows), showing that the whole gouge layer was recovered and no PSS was lost during sample preservation. (b) Sample phv354 sheared only at high velocity (1 m/s) for a total displacement of ~6 m. Compared to the dry samples, deformation is homogeneously distributed across the gouge layer. (c) Zoom of the zone marked in (b) where the PSS typically develops in dry samples shows a reduced porosity and incipient shear band (arrows).

in Figure 6, this effective-stress law contains the effective-stress coefficient, α, as the weighting parameter between normal stress σ_n and pore pressure p_f. We fit this relation to our experimental data employing a singular-value decomposition yielding uncertainties of the fit parameters (Sotin & Poirier, 1984). The effective-stress law obtained by fitting the experimental data is illustrated by the isolines in Figure 11, which show the shear stress as a function of normal stress and pore fluid pressure. Symbols in Figure 11 show the experimental data, where both the symbol color and size represent the value of the experimentally measured shear stress. The match of colors of isolines and symbols in the graphical representation of the effective-stress law reflects that the model fits the data within their error (Figure 11). The uncertainties of the fit parameters are all within 1.5% (Table 3). The data from saturated experiments for the low-velocity step ($v_1 = 1$ mm/s) are fit with $\mu = 0.71 \pm 0.01$ and $\alpha = 1.03 \pm 0.01$ (Figure 11a, Table 3). Thus, the additional fit parameter, α, in Equation 3 does not have a large effect on the result for the coefficient of friction compared to that obtained from using Equation 2 ($\mu_{sat} = 0.69$). Fit parameters for the high-velocity step ($v_2 = 1$ m/s) are $\mu = 0.70 \pm 0.01$ and $\alpha = 0.96 \pm 0.01$ for the peak-stress data (Figure 11b), and $\mu = 0.19 \pm 0.00$ and $\alpha = 0.96 \pm 0.02$ for the steady-state shear-stress data (Figure 11c), which might be affected by poor drainage potentially yielding an overestimation of the friction coefficient. Again, the coefficient of friction is similar to the values obtained from fitting Equation 2 ($\mu_{sat} = 0.68$ and $\mu_{sat,ss} = 0.17$ for peak and steady-state shear stress, respectively, Figure 6). The low friction coefficient for the steady-state phase reflects that shear stress is relatively independent of effective normal stress.

The values obtained for the coefficient of friction by fitting the experimental data with relation (3) as well as with relation (2) are in line with those of previous experimental studies (e.g., Rempe et al., 2017; Verberne,
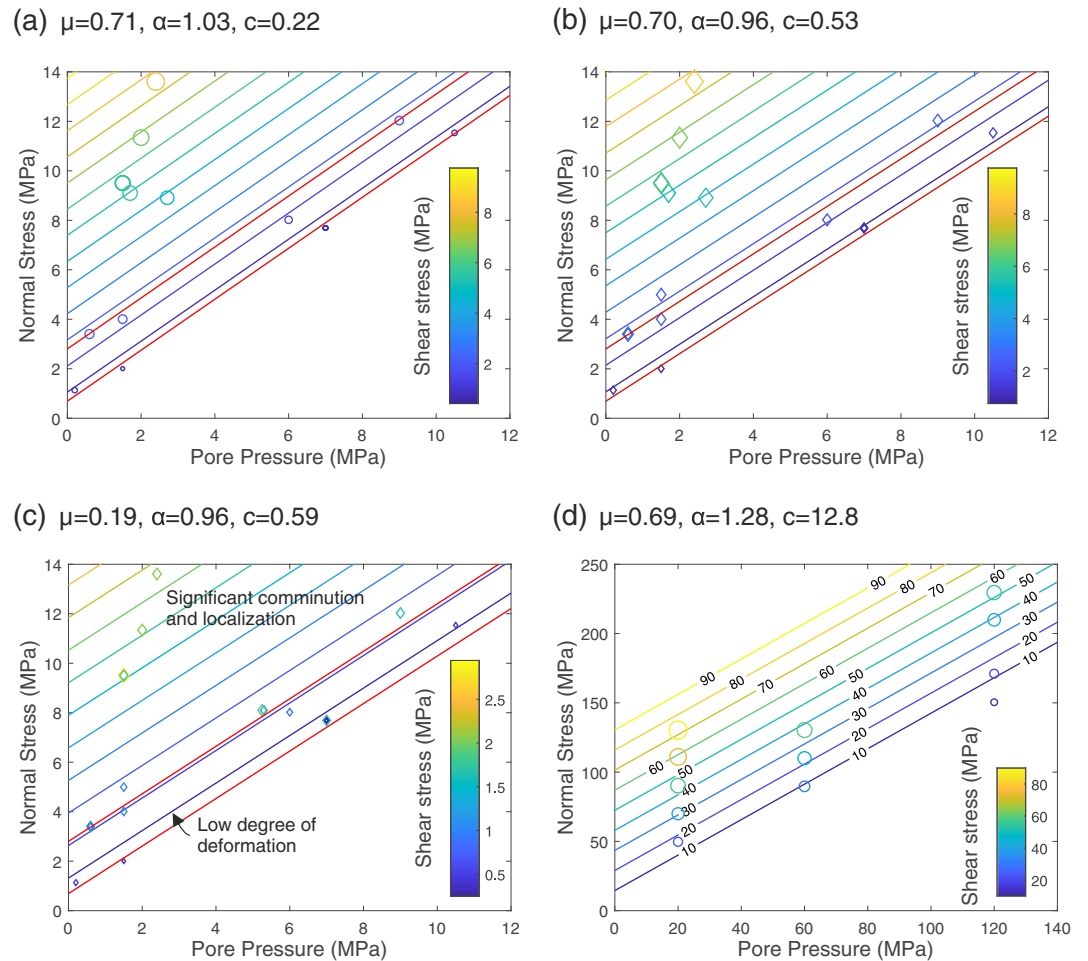
Figure 11. Shear stress as a function of pore pressure and normal stress according to the effective-stress laws. Color and size of symbols represent the value of the experimentally measured shear stress. Isolines show best fit of the effective-stress law for shear stress (given in titles of subplots and Table 3) to experimental data. Therefore, if the effective-stress law represented by the lines fits the experimental data perfectly, symbols will have the exact color of the lines on which they plot. (a) Steady-state shear stress during low-velocity step. (b) Peak shear stress and (c) steady-state shear stress during high-velocity step. The fit to the steady-state shear stress data from the high-velocity step (c) is relatively poor, which is an expected result as significant weakening of the gouges occurred independently of the applied effective normal stress. (d) Data from Kurzawski et al. (2016). Red lines in (a)–(c) correspond to constant effective normal stress of $\sigma_{n,eff} = 0.7$ MPa and $\sigma_{n,eff} \geq 2.8$ MPa and represent the different microstructural domains, that is, a low degree of deformation at 0.7 MPa and significant comminution and localization at higher effective normal stresses (compare red lines in Figure 12).

Table 3
Best Fit Parameters for the Effective-Stress Law Obtained by Singular Value Decomposition

	Low-velocity step (steady state)		High-velocity step (peak stress)		High-velocity step (steady state)		Kurzawski et al. (2016)	
	Dry	Saturated	Dry	Saturated	Dry	Saturated	20°C	140°C
μ	0.79 ± 0.09	0.71 ± 0.01	0.91 ± 0.1	0.71 ± 0.01	—	0.19 ± 0.00	0.64 ± 0.05	0.50 ± 0.03
α	—	1.03 ± 0.01	—	0.96 ± 0.01	—	0.96 ± 0.02	1.28 ± 0.04	1.09 ± 0.03
c (MPa)	0.17 ± 0.44	0.22 ± 0.03	0.08 ± 0.34	0.53 ± 0.04	—	0.59 ± 0.02	12.8 ± 2.7	0.03 ± 1.54

Note. The analysis assumed a linear variation of shear stress with effective normal stress with constants μ and α. No good fit was obtained for steady-state shear stress data from high-velocity step on dry gouges.

Plümper, et al., 2014). Notably, the effective-stress coefficient α is close to unity for all cases, as also observed for the shear strength of clay-bearing gouges (e.g., Morrow et al., 1992). An effective-stress coefficient $\alpha \approx 1$ was also indirectly observed by Scuderi and Collettini (2016), who found that the pore fluid factor, that is, the ratio of controlled pore fluid pressure to applied normal stress, does not affect the steady-state shear strength of carbonate gouges sheared at low velocity. As the effective-stress coefficient is close to unity, the effective-stress law (3) reduces to the Coulomb law (2). Thus, the effective normal stress can be taken as equal to the Terzaghi stress when discussing the shear stress of carbonate gouges. In the following, we will therefore use the term *effective normal stress* instead of *Terzaghi stress*.

The range of normal stresses and pore fluid pressures we applied in our experimental study is rather limited ($\sigma_n = 1.3$ to 13.6 MPa, $p_f = 0.2$ to 10.5 MPa). Reevaluating data from Kurzawski et al. (2016), who performed low-velocity (μm/s) friction experiments on fluid-pressurized carbonate gouges with normal stresses ranging from 30 to 110 MPa, extends our range in normal and pore fluid pressures. Analyzing the data by Kurzawski et al. (2016) in the light of the effective-stress law (3) yields a constant $\mu = 0.64 \pm 0.05$, very similar to the value obtained for the experiments performed in this study, and $\alpha = 1.28 \pm 0.04$, an effective-stress coefficient significantly larger than unity, unlike the estimate made from our experimental data (Table 3, Figure 11d). Kurzawski et al. (2016) assumed that differences in the shear stress for experiments performed at different pore fluid pressures were due to differences in the "internal" coefficient of friction rather than due to $\alpha \neq 1$ and reported that the "internal" coefficient of friction for their gouge material (>85 wt.% carbonate) sheared at room temperature decreases from 0.84 to 0.58 as the pore fluid pressure is increased from 20 to 120 MPa. On the one hand, friction might be governed by friction on an interface for the kind of the microstructures presented by Kurzawski et al. (2016), that is, intense grain size reduction within a Riedel shear zone containing a discrete "microfault," and mirror-like slip surfaces. For the friction between two contacting surfaces, an effective-stress coefficient $\alpha \approx 1$ is interpreted to arise from real areas of contact A_r being much smaller than the total area A since pore pressure acts only on the area of an interface that is not in contact resulting in $\alpha = 1 - A_r/A$ (Hirth & Beeler, 2015; Scholz, 2002). On the other hand, the friction coefficient of 0.84 reported by Kurzawski et al. (2016) appears to be high in comparison with other low-velocity studies on water-saturated calcite gouges (Verberne, Plümper, et al., 2014), lending support to the appropriateness of our effective-stress approach. Therefore, the effective-stress coefficient is possibly a function of normal stress and/or pore fluid pressure and might exceed 1 at relatively high normal stresses.

4.3. Role of Thermal Pressurization and High-Temperature Deformation Mechanisms in Fault Weakening

4.3.1. Subseismic Slip Rates (1 mm/s)

During the low-velocity stage in our experiments, the steady-state shear stress was lower for fluid-saturated than for dry gouges (Figure 3a). The same observation was made in previous experiments on water-saturated gouges sheared at subseismic velocity (0.03–100 μm/s), and this effect was attributed to increased intergranular lubrication, subcritical cracking and/or pressure solution (Verberne, Plümper, et al., 2014), all processes that possibly occur in our experiments performed at 1 mm/s. The relatively high degree of axial compaction in the presence of pressurized fluids compared to dry gouges (Figure 3c) is consistent with a higher degree of gouge particle fracturing due to enhanced subcritical crack growth. Efficient intergranular lubrication lowering friction between particles may be responsible for the slightly lower degree of frictional heating relative to dry gouges (Figure 3d), which in turn indicates that the observed fluid pressure increase in the volume-controlled experiments (Figure 3e) is a mechanical effect, that is, it is due to the observed compaction of the pore space rather than thermal pressurization. Due to the good drainage of the gouges during the low-velocity stage, thermal expansion of the fluids in the pore space cannot result in pressure changes. In addition, thermal pressurization would likely have resulted in dilation, not the observed compaction. The mechanical pressurization in the volume-controlled experiments leads to a decrease in the shear stress by the same order of magnitude as the fluid pressure increase (Figure 3a) and to a constant friction coefficient (Figure 3b), which supports our previous conclusion that the effective-stress coefficient is close to unity.

4.3.2. Seismic Slip Rates (1 m/s)

4.3.2.1. Dynamic-Weakening Phase

The acceleration of the onset of dynamic weakening in fluid-saturated gouges in comparison to dry gouges (Figures 4 and 5) is consistent with the behavior previously observed in cohesive carbonate rocks and water-dampened calcite gouges sheared at ≥ 1 m/s leading to the conclusion that the presence of fluids facilitates

earthquake nucleation in carbonate rocks. In cohesive rocks, the accelerated weakening was previously attributed to brittle failure of asperities associated with enhanced dissolution processes (Violay et al., 2013, 2015). It has also been suggested that flash weakening is the result of dislocation avalanches and other microphysical processes associated to shock waves, resulting in CO_2 release, nanograin formation, and amorphization of carbon, processes that may lubricate a fault (Spagnuolo et al., 2015). In fluid-saturated calcite gouges sheared at 1 m/s, enhanced subcritical crack growth—taking effect already during sample preparation and loading of the sample—and intergranular lubrication have been invoked to play a role for the dynamic weakening (Rempe et al., 2017). Similar processes have been proposed to be active at lower sliding velocities (Verberne, Plümper, et al., 2014).

Thermal pressurization was ruled out as an efficient weakening mechanism for cohesive carbonate rocks, based on the lack of decarbonation and modest thermal expansion of pore fluids during the deformation of cohesive carbonate rocks (Violay et al., 2013, 2015). Chen et al. (2017) suggested, however, that pore water vaporization contributed to the observed slip weakening. Our evaluation of the drainage state of the gouges suggests that conditions are drained at the initiation of sliding at high velocity and our mechanical data do not indicate that thermal pressurization is responsible for accelerated dynamic weakening, either. Neither compaction nor a temperature rise that might act as mechanisms for pressurization are observed at this early point in the experiment. A fluid pressure rise (Figure 4j) and transient dilation (Figure 4f)—a proxy for pore fluid pressurization—are only observed once temperatures start to increase at ~0.5 m of displacement, subsequent to the onset of dynamic weakening (Figure 4h). Thus, we can exclude thermal pressurization as the dominant weakening mechanism for calcite gouges sheared at seismic velocity and attribute the weakening of gouges sheared in the presence of pressurized pore fluids to the same weakening mechanisms invoked to play a role in dry and merely saturated gouges and cohesive rocks, that is, brittle fracture of asperities/cataclasis of clasts, subcritical crack growth, intergranular lubrication or microphysical processes associated to shock waves (Rempe et al., 2017; Smith et al., 2015; Spagnuolo et al., 2015; Verberne, Plümper, et al., 2014; Violay et al., 2013, 2015).

4.3.2.2. "Steady-State" Phase

After the first 4 m of slip at high velocity, a perfect steady state has not been reached; instead, shear stress continues to evolve slightly while temperatures rise and—in volume-controlled saturated experiments—fluid-pressures continue to increase. This continued evolution of shear stress might be due to (partially) undrained conditions (section 4.2) or alternatively a change in the microdeformation mechanism with temperature. During this "steady-state" phase, the shear stress is generally low, especially for dry gouges (Figures 4a, 4b, and 6b). Although temperature increases by the same amount for dry and saturated conditions in experiments performed at an effective normal stress of ~8 MPa (Figure 4g), the high temperatures might have different effects depending on the presence or absence of pore fluids. Gouges sheared in volume-controlled fluid pressure conditions dilate (Figures 4e and 4f) and show an increase in pore fluid pressure with slip (Figures 4i and 4j) that we attribute to thermal pressurization, because temperature increases by ~200–400°C (Figures 4g and 4h) during the 4 m of displacement of the high-velocity step. In fluid pressure-controlled experiments, the relatively low degree of compaction might suggest that elevated pore fluid pressures caused by thermal pressurization counteract shear compaction that occurs by a much higher degree in dry gouges.

Shear stress in the phase following dynamic weakening has been proposed to be controlled by a powder lubrication mechanism (Han et al., 2010; Reches & Lockner, 2010; Tisato et al., 2012), because of the presence of ultrafine materials (nanopowders) in the slipping zone that may accommodate slip by rolling (Han, Shimamoto, Hirose, et al., 2007; Spagnuolo et al., 2015; Tisato et al., 2012; Violay et al., 2013, 2014). However, powder lubrication cannot explain the strong "healing" or increase in shear stress with deceleration of sliding velocity at the end of a friction experiment (Violay et al., 2019). As a consequence, crystal-plastic processes, which may be grain size-, temperature, and strain rate dependent, may control the shear stress in the steady-state phase (Demurtas et al., 2019; De Paola et al., 2015; Green et al., 2015; Pozzi et al., 2019; Spagnuolo et al., 2015; Violay et al., 2019). Microstructural features such as aggregates of equiaxial nanograins with polygonal texture exhibiting no crystallographic preferred orientation and low dislocation density are indicative of superplastic behavior and the operation of grain-boundary sliding (GBS) mechanisms (De Paola et al., 2015; Green et al., 2015; Schmid et al., 1977; Verberne et al., 2014; Walker et al., 1990). Dynamically recrystallized grains and crystallographic preferred orientations reminiscent of ultramylonites

were observed in calcite gouges recovered after shearing at a slip rate of 1.4 m/s and normal stress of 25 MPa (Pozzi et al., 2019). Pozzi et al. (2019) concluded that these textures developed due to several competing temperature-dependent deformation mechanisms. Relying on previously published flow laws (Ashby & Verrall, 1973; Schmid et al., 1977; Walker et al., 1990), De Paola et al. (2015) estimated a pressure-independent flow stress agreeing within 1 order of magnitude with the experimentally-observed shear stress values.

In our experiments performed at effective normal stresses ≥2.8 MPa, evidence for the occurrence of crystal-plastic deformation can be found in the microstructures and the mechanical data. First, elongated recrystallized grains lining the principal slip surfaces indicate that crystal-plastic processes played a role in the deformation of the gouges. The presence of sintered and recrystallized grains along the slip surface and evidence of decarbonation (Figures 7–9) suggest that temperatures within the principal slip zone locally exceeded the measured values (>720°C in dry conditions; e.g., Han, Shimamoto, Ando, et al., 2007), possibly reaching temperatures needed to yield a flow stress in the order of a few MPa as estimated by De Paola et al. (2015). Only in experiments performed at 1 MPa temperatures remain relatively low (≤50 °C) and there is no microstructural evidence for crystal-plastic deformation. Furthermore, the relation between strain rate and flow stress for crystal-plastic deformation processes is independent of normal stress. In our experiments on dry gouges, shear stress is in fact independent of effective normal stress as reflected by the friction coefficient close to zero ($\mu = -0.03$; Figure 6b). Fluid-saturated gouges exhibit a weak dependence of shear stress on effective normal stress ($\mu = 0.18$; Table 3) compared to the effective normal-stress dependence of the peak stress ($\mu = 0.67$) or the steady-state shear stress during the low-velocity step ($\mu = 0.70$). The difference in the absolute value of shear stress in dry and water-saturated gouges observed in the experiments performed at ~8 MPa (Figures 4a–4d and Figure 6b) might be associated with a slightly smaller grain size in dry compared to water-saturated gouges, although we do not observe such a grain size difference. In previous studies, no significant effect of the presence of pore water was found on the rheology of cohesive carbonate rocks determined in experiments at elevated temperatures (De Bresser et al., 2005; Rutter, 1974) or on the recrystallization behavior as deduced from natural microstructures (Schenk et al., 2005). It thus remains unclear whether the increase in steady-state shear stress in the presence of water is consistent with crystal-plastic deformation.

In summary, thermal pressurization likely occurs during "steady-state" shearing at seismic velocity, but as shear stress and friction coefficient are low at this stage, thermal pressurization has a negligible effect on the evolution of shear stress. Instead, the combination of the negligible dependence of shear stress on effective normal stress and microstructural observations of sintered and recrystallized grains and evidence for decarbonation supports the conclusion of previous studies that high-temperature deformation mechanisms, such as grain-boundary sliding, play a role in the deformation of calcite gouges sheared at high velocity.

4.4. Influence of Effective Normal Stress and Fluid Pressure on Slip Localization

Two types of microstructures developed in the calcite gouges sheared at seismic slip rates, dependent on the applied effective normal stress (Figure 12). We observed that the degree of deformation and localization was negligible at a low effective normal stress of 1 MPa (Figure 10) but high at effective normal stresses ≥2.8 MPa (Figures 7–9 and 12). The small degree of deformation of gouges sheared at low effective normal stress (microstructural Domain 1 in Figures 10 and 12) is associated with low shear stress and moderate frictional heating (Figure 5), while the relatively high degree of deformation and localization observed in gouges sheared at higher effective normal stress was associated with relatively high shear stress, resulting in the observed high degree of frictional heating in dry as well as saturated gouges (Figures 3–5). In turn, this high degree of localization caused recrystallization, sintering, and decarbonation of the calcite gouges in a zone adjacent to the principal slip surface(s) (Figures 8c and 9c). In a sample sheared at seismic slip rates and an effective normal stress of 3 MPa but relatively high pore fluid pressure (9 MPa, phv350), three textural zones developed during shear. However, since no evidence of recrystallization or sintering was observed, the deformation in textural Zone 3 appears to be less intense than in gouges deformed at the same effective normal stress (cf. Figure 8g to Figures 8a–8f). Possibly, the degree of deformation and localization, to first order controlled by the effective normal stress, is influenced to some degree by the absolute value of the pore fluid pressure as well. Notably, the mechanical data do not show this independent effect of the pore fluid
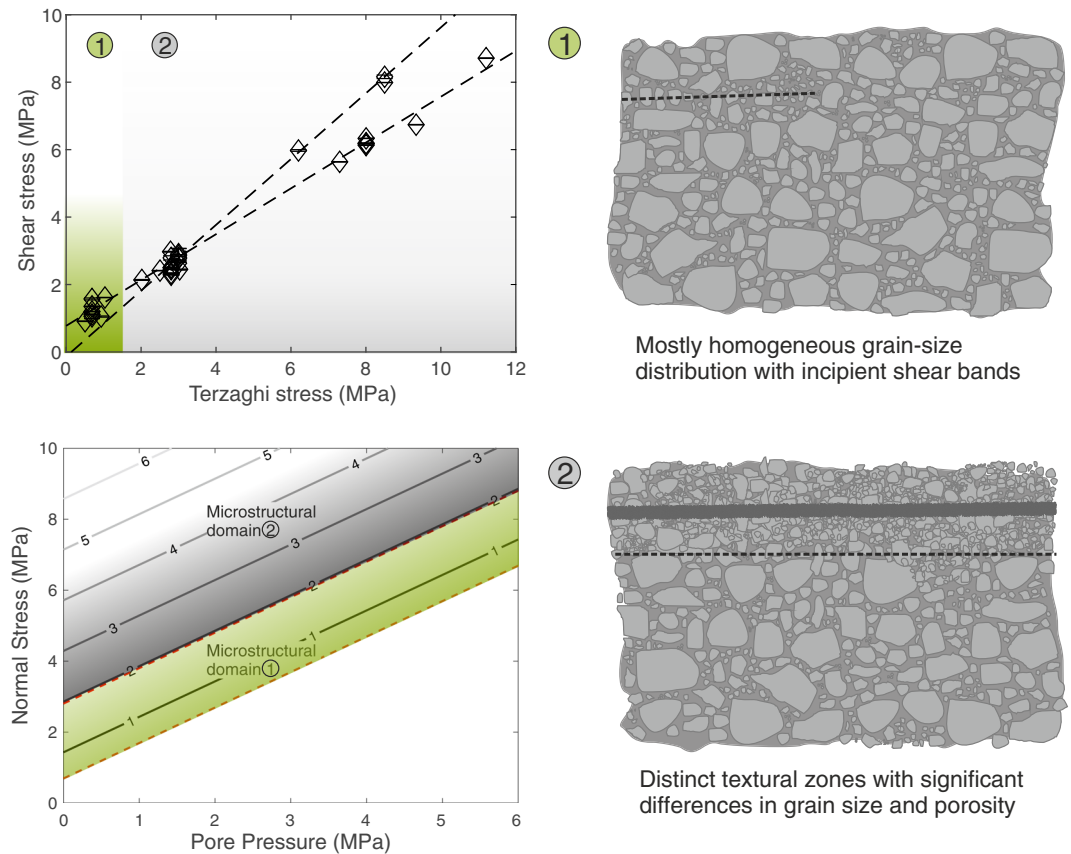
Figure 12. Summary figure. Development of two microstructural domains in calcite gouges sheared at seismic slip rate as a function of Terzaghi stress (like Figure 6) and in the normal stress pore pressure space (like Figure 11), highlighted by gray (microstructural Domain 1) and green background (microstructural Domain 2). Textural characteristics for Domains 1 and 2 are sketched on the right.

pressure, but appear to solely depend on effective normal stress without being modulated by pore fluid pressure, that is, $\alpha \approx 1$.

An influence of the effective normal stress on the microstructural evolution or frictional behavior was observed in several experimental studies in gouges of various lithologies. Microstructures similar to those that we observed at normal stresses >2.8 MPa—localization to shear bands or principal slip surfaces as well as recrystallized or sintered material—were described for gouge layers sheared at a broad range of slip rates (μm/s to m/s), normal stresses (a few to tens of MPa), and total displacements (mm to m) (e.g., Carpenter et al., 2016; Chen et al., 2017; Smith et al., 2013; Verberne, Plümper, et al., 2014). Carpenter et al. (2016) observed that the degree of comminution and localization in calcite gouge layers increased with increasing normal stress. Consistent with these findings by Carpenter et al. (2016), Smith et al. (2015) found that the strengthening phase prior to dynamic weakening of calcite gouges became progressively shorter at higher normal stress, indicative of an increasingly rapid localization process. An effect of the normal stress on the degree of comminution was also observed in shearing experiments on quartz gouges (Mair & Marone, 1999). However, gouges showing negligible grain size reduction or strain localization, like in microstructural domain 1 (Figure 12), have not previously been described. In many of the previous experimental studies, the gouges were saturated with water, but the fluids were not pressurized. It is therefore likely that the particular microstructures presented in this study (Figures 10 and 12) are the result of the low effective normal stress and the presence of pressurized fluids enhancing intergranular lubrication. The limited degree of slip localization at low effective normal stresses limits frictional heating and prevents mechanisms such as thermal pressurization, crystal-plasticity and other temperature-dependent mechanisms from taking effect. The formation of ultra-polished slip surfaces—a common feature in fault zones cutting carbonates

(Demurtas et al., 2016; Fondriest et al., 2013; Ohl et al., 2020; Pozzi et al., 2018; Siman-Tov et al., 2013)—under very low effective normal stress (e.g., faults cutting unconsolidated gravels at depths <50 m) is likely the result of pressure solution processes rather than the propagation of seismic ruptures up to the surface (Demurtas et al., 2020). The low effective stress at shallow depth or at larger depth but high pore fluid pressure likely renders faults in carbonate rocks mechanically weak. At larger depth and relatively dry conditions, carbonate rocks are inherently strong but may weaken due to thermally-induced mechanisms.

5. Conclusions

A series of intermediate- (1 mm/s) to high- (1 m/s) velocity, rotary-shear experiments on room-dry and water-saturated calcite gouges was conducted to test (i) the drainage conditions during shear and (ii) the effective-stress dependence of shear strength for carbonate gouges as a prerequisite to further analyze the experimental data, as well as (iii) the dependence of shear strength and (iv) microstructural evolution on normal stress and pore fluid pressure.

1. Evaluation of drainage conditions is a prerequisite for the determination of the effective-stress dependence of shear strength. When assessing the drainage state of the gouges, the effect of shear heating has to be taken into account: Evaluation of the temperature- and pressure-dependence of hydraulic diffusivity of the water-saturated gouges shows that the temperature increase may affect the hydraulic diffusivity more than changes in their permeability and porosity due to the microstructural evolution (Figure 2). As characteristic times are short compared to the time required to reach quasi steady-state behavior and to the duration of the steady-state phase, we conclude that our gouges sheared at 1 mm/s are drained, while we cannot exclude partially undrained conditions in gouges sheared at 1 m/s, where characteristic times are relatively long. Experimental data gathered at slip velocities exceeding 1 m/s are almost certainly affected by poor drainage, that is, the actual pore fluid pressure is unknown. To better resolve pore fluid pressures, the development of techniques to measure local pore fluid pressure during high-velocity friction experiments is critical (Brantut, 2020; Proctor et al., 2019). In natural fault zones, permeability creation during earthquake slip (Sibson, 1992) might result in improved drainage of pressurized fluids from the slipping zone. However, drainage conditions in natural fault zones ultimately depend on pressure and temperature conditions.

2. Evaluation of the effective-stress law for shear stress yields an effective-stress coefficient $\alpha \approx 1$ for all phases of sliding and independent of the sliding velocity. An effective-stress coefficient for shear stress close to unity is consistent with some previous studies on clay-bearing gouges. Analysis of data from a previous experimental study on calcite gouges indicates that $\alpha > 1$ for gouges deformed at lower sliding velocity and higher effective normal stress than explored here, possibly due to advanced comminution and localization. Therefore, the effective-stress dependence of shear stress might vary with depth or the maturity of faults, a hypothesis that warrants further testing.

3. Our experimental setup allowing the measurement of pore fluid pressure is predestined to evaluate the effect of thermal pressurization on the shear strength of the gouges. At low sliding velocity (1 mm/s), no evidence of thermal pressurization was found. As suggested in previous studies, the observed reduction of steady-state shear stress due to the presence of pressurized fluids is likely related to an enhancement of the kinetics of subcritical crack growth or intergranular lubrication (Verberne, Plümper, et al., 2014; Violay et al., 2013, 2015). When sheared at 1 m/s, fluid-saturated gouges exhibit accelerated dynamic weakening compared to dry gouges. Thermal pressurization—evidenced by a fluid-pressure increase associated with a rise in temperature and dilation—is likely occurring only after this dynamic weakening. Even then, thermal pressurization is found to have a negligible effect on shear strength because dynamic weakening led to a vanishing friction coefficient ($\mu \rightarrow 0$) and thus to a loss of the overall effective-stress dependence of shear stress. Likely, pressure-independent crystal-plastic deformation mechanisms are active, as indicated by the presence of dynamically recrystallized grains in the principal slip zones. Thus, the evolution of shear stress during high-velocity sliding documents the transition from pressure-controlled to temperature-controlled slip behavior.

4. The degree of comminution and slip localization in sheared calcite gouges increases with increasing effective normal stress. The degree of comminution is very low at stresses <1 MPa, while a substantial degree of comminution and localization of slip to one or more slip surfaces are observed in samples sheared at effective normal stresses of ~3 MPa and higher (Figure 12). Consistent with the differing

degree of localization, frictional heating is negligible at low effective normal stresses, but significant at higher stresses (≥ 2.8 MPa). Therefore, in nature, thermal pressurization is unlikely to occur at very shallow depth or for high initial pore fluid pressures resulting in low effective normal stresses. However, as our experiments revealed, even in cases where frictional heating caused a temperature rise of several hundred degrees, thermal pressurization was found to have a negligible effect on both timing of dynamic weakening and magnitude of the steady-state shear stress.

Notation

p_f	Pore fluid pressure (Pa), servo-controlled
$\sigma_n = F/A$	Normal stress (experimental parameter depending on servo-controlled applied force F and cross-sectional area A; Pa)
$\sigma_T = \sigma_n - p_f$	Terzaghi (normal) stress (Pa)
$\sigma_{eff} = \sigma_n - \alpha p_f$	Effective normal stress (Pa)
α	Effective-stress coefficient for frictional strength (−)
μ	Coefficient of friction (−)
$\tau = \mu \sigma_{eff} + c$	Shear stress (Pa)
c	Cohesion (Pa)
$k = Q\eta / \Delta p_f A$	Permeability (m^2)
Q	Flow rate (m^3/s)
η	Fluid viscosity (Pas)
A	Cross-sectional area of the sample (m^2)
Δp_f	Fluid-pressure gradient (Pa)
$D_{hyd} = k/\eta s$	Hydraulic diffusivity (m^2/s)
$s \sim \phi c_{H_2O}$	Specific storage capacity (1/Pa)
ϕ	Porosity
c_{H_2O}	Compressibility of the pore fluid (1/Pa)
c_{pp}	Compressibility of the pore space (1/Pa)
l_{char}, t_{char}	Characteristic length and time, respectively, of the diffusion process

Data Availability Statement

Experimental data are available via Mendeley Data (Rempe et al., 2020).

References

Andrews, D. J. (2002). A fault constitutive relation accounting for thermal pressurization of pore fluid. *Journal of Geophysical Research*, *107*(B12), 2363. https://doi.org/10.1029/2002JB001942

Ashby, M., & Verrall, R. (1973). Diffusion-accommodated flow and superplasticity. *Acta Metallurgica*, *21*(2), 149–163. https://doi.org/10.1016/0001-6160(73)90057-6

Badt, N. Z., Tullis, T. E., Hirth, G., & Goldsby, D. L. (2020). Thermal pressurization weakening in laboratory experiments. *Journal of Geophysical Research: Solid Earth*, *125*, e2019JB018872. https://doi.org/10.1029/2019JB018872

Beeler, N., Tullis, T., Blanpied, M., & Weeks, J. (1996). Frictional behavior of large displacement experimental faults. *Journal of Geophysical Research*, *101*(B4), 8697–8715. https://doi.org/10.1029/96JB00411

Brantut, N. (2020). Dilatancy-induced fluid pressure drop during dynamic rupture: Direct experimental evidence and consequences for earthquake dynamics. *Earth and Planetary Science Letters*, *538*, 116179. https://doi.org/10.1016/j.epsl.2020.116179

Brantut, N., Schubnel, A., Rouzaud, J. N., Brunet, F., & Shimamoto, T. (2008). High-velocity frictional properties of a clay-bearing fault gouge and implications for earthquake mechanics. *Journal of Geophysical Research*, *113*, B10401. https://doi.org/10.1029/2007JB005551

Bullock, R. J., De Paola, N., Holdsworth, R. E., & Trabucho-Alexandre, J. (2014). Lithological controls on the deformation mechanisms operating within carbonate-hosted faults during the seismic cycle. *Journal of Structural Geology*, *58*, 22–42. https://doi.org/10.1016/j.jsg.2013.10.008

Carpenter, B., Collettini, C., Viti, C., & Cavallo, A. (2016). The influence of normal stress and sliding velocity on the frictional behaviour of calcite at room temperature: Insights from laboratory experiments and microstructural observations. *Geophysical Supplements to the Monthly Notices of the Royal Astronomical Society*, *205*(1), 548–561. https://doi.org/10.1093/gji/ggw038

Chen, J., Niemeijer, A., Yao, L., & Ma, S. (2017). Water vaporization promotes coseismic fluid pressurization and buffers temperature rise. *Geophysical Research Letters*, *44*, 2177–2185. https://doi.org/10.1002/2016GL071932

Chiarabba, C., Amato, A., Anselmi, M., Baccheschi, P., Bianchi, I., Cattaneo, M., et al. (2009). The 2009 L'Aquila (central Italy) M_W6. 3 earthquake: Main shock and aftershocks. *Geophysical Research Letters*, *36*, L18308. https://doi.org/10.1029/2009GL039627

De Bresser, J. H. P., Urai, J. L., & Olgaard, D. L. (2005). Effect of water on the strength and microstructure of Carrara marble axially compressed at high temperature. *Journal of Structural Geology*, *27*(2), 265–281. https://doi.org/10.1016/j.jsg.2004.10.002

De Paola, N., Holdsworth, R. E., Viti, C., Collettini, C., & Bullock, R. (2015). Can grain size sensitive flow lubricate faults during the initial stages of earthquake propagation? *Earth and Planetary Science Letters*, *431*, 48–58. https://doi.org/10.1016/j.epsl.2015.09.002

Delle Piane, C., Clennell, M. B., Keller, J. V., Giwelli, A., & Luzin, V. (2017). Carbonate hosted fault rocks: A review of structural and microstructural characteristic with implications for seismicity in the upper crust. *Journal of Structural Geology*, *103*, 17–36. https://doi. org/10.1016/j.jsg.2017.09.003

Delle Piane, C., Giwelli, A., Clennell, M. B., Esteban, L., Kiewiet, M. C. D. N., Kiewiet, L., et al. (2016). Frictional and hydraulic behaviour of carbonate fault gouge during fault reactivation—An experimental study. *Tectonophysics*, *690*, 21–34. https://doi.org/10.1016/j. tecto.2016.07.011

Demurtas, M., Balsamo, F., & Pizzati, M. (2020). Signature of coseismic slip in unconsolidated Quaternary gravels, Campo Imperatore, Italy. In *EGU General Assembly 2020*, Online, 4–8 May 2020, EGU2020-7192. https://doi.org/10.5194/egusphere-egu2020-7192

Demurtas, M., Fondriest, M., Balsamo, F., Clemenzi, L., Storti, F., Bistacchi, A., & Di Toro, G. (2016). Structure of a normal seismogenic fault zone in carbonates: The Vado di Corno fault, Campo Imperatore, central Apennines (Italy). *Journal of Structural Geology*, *90*, 185–206. https://doi.org/10.1016/j.jsg.2016.08.004

Demurtas, M., Smith, S. A., Prior, D. J., Brenker, F. E., & Di Toro, G. (2019). Grain size sensitive creep during simulated seismic slip in nanogranular fault gouges: Constraints from transmission Kikuchi Diffraction (TKD). *Journal of Geophysical Research: Solid Earth*, *124*, 10,197–10,209. https://doi.org/10.1029/2019JB018071

Ferri, F., Di Toro, G., Hirose, T., & Shimamoto, T. (2010). Evidence of thermal pressurization in high-velocity friction experiments on smectite-rich gouges. *Terra Nova*, *22*(5), 347–353. https://doi.org/10.1111/j.1365-3121.2010.00955.x

Fondriest, M. (2014). *Structure and mechanical properties of seismogenic fault zones in carbonates* (PhD thesis). Padua, Italy: Università degli Studi di Padova.

Fondriest, M., Smith, S. A., Candela, T., Nielsen, S. B., Mair, K., & Di Toro, G. (2013). Mirror-like faults and power dissipation during earthquakes. *Geology*, *41*(11), 1175–1178. https://doi.org/10.1130/G34641.1

Green, H. W. I., Shi, F., Bozhilov, K., Xia, G., & Reches, Z. (2015). Phase transformation and nanometric flow cause extreme weakening during fault slip. *Nature Geoscience*, *8*(6), 484–489. https://doi.org/10.1038/ngeo2436

Han, R., Hirose, T., & Shimamoto, T. (2010). Strong velocity weakening and powder lubrication of simulated carbonate faults at seismic slip rates. *Journal of Geophysical Research*, *115*, B03412. https://doi.org/10.1029/2008JB006136

Han, R., Shimamoto, T., Ando, J.-I., & Ree, J.-H. (2007). Seismic slip record in carbonate-bearing fault zones: An insight from high-velocity friction experiments on siderite gouge. *Geology*, *35*(12), 1131. https://doi.org/10.1130/g24106a.1

Han, R., Shimamoto, T., Hirose, T., Ree, J.-H., & Ando, J.-I. (2007). Ultralow friction of carbonate faults caused by thermal decomposition. *Science*, *316*(5826), 878–881. https://doi.org/10.1126/science.1139763

Hartmann, J., & Moosdorf, N. (2012). The new global lithological map database GLiM: A representation of rock properties at the earth surface. *Geochemistry, Geophysics, Geosystems*, *13*, Q12004. https://doi.org/10.1029/2012GC004370

Hirose, T., & Shimamoto, T. (2005). Growth of molten zone as a mechanism of slip weakening of simulated faults in gabbro during frictional melting. *Journal of Geophysical Research*, *110*, B05202. https://doi.org/10.1029/2004JB003207

Hirth, G., & Beeler, N. M. (2015). The role of fluid pressure on frictional behavior at the base of the seismogenic zone. *Geology*, *43*(3), 223–226. https://doi.org/10.1130/g36361.1

Kurzawski, R. M., Niemeijer, A. R., Stipp, M., Charpentier, D., Behrmann, J. H., & Spiers, C. J. (2018). Frictional properties of subduction input sediments at an erosive convergent continental margin and related controls on décollement slip modes: The Costa Rica seismogenesis project. *Journal of Geophysical Research: Solid Earth*, *123*, 8385–8408. https://doi.org/10.1029/2017JB015398

Kurzawski, R. M., Stipp, M., Niemeijer, A. R., Spiers, C. J., & Behrmann, J. H. (2016). Earthquake nucleation in weak subducted carbonates. *Nature Geoscience*, *9*(9), 717–722. https://doi.org/10.1038/ngeo2774

Lachenbruch, A. H. (1980). Frictional heating, fluid pressure, and the resistance to fault motion. *Journal of Geophysical Research*, *85*(B11), 6097–6112. https://doi.org/10.1029/JB085iB11p06097

Mair, K., & Marone, C. (1999). Friction of simulated fault gouge for a wide range of velocities and normal stresses. *Journal of Geophysical Research*, *104*(B12), 28,899–28,914. https://doi.org/10.1029/1999JB900279

Mase, C. W., & Smith, L. (1987). Effects of frictional heating on the thermal, hydrologic, and mechanical response of a fault. *Journal of Geophysical Research*, *92*(B7), 6249. https://doi.org/10.1029/JB092iB07p06249

Miller, S. (2002a). Earthquake scaling and the strength of seismogenic faults. *Geophysical Research Letters*, *29*(10), 27-1–27-4. https://doi. org/10.1029/2001GL014181

Miller, S. A. (2002b). Properties of large ruptures and the dynamical influence of fluids on earthquakes and faulting. *Journal of Geophysical Research*, *107*(B9), 2182. https://doi.org/10.1029/2000JB000032

Miller, S. A. (2013). The role of fluids in tectonic and earthquake processes. In *Advances in geophysics* (pp. 1–46). Amsterdam, The Netherlands: Elsevier. https://doi.org/10.1016/B978-0-12-380940-7.00001-9

Miller, S. A., Collettini, C., Chiaraluce, L., Cocco, M., Barchi, M., & Kaus, B. J. (2004). Aftershocks driven by a high-pressure CO_2 source at depth. *Nature*, *427*(6976), 724–727. https://doi.org/10.1038/nature02251

Mitchell, T. M., Smith, S. A. F., Anders, M. H., Di Toro, G., Nielsen, S., Cavallo, A., & Beard, A. D. (2015). Catastrophic emplacement of giant landslides aided by thermal decomposition: Heart Mountain, Wyoming. *Earth and Planetary Science Letters*, *411*, 199–207. https:// doi.org/10.1016/j.epsl.2014.10.051

Moore, D., Jin, M., Summers, R., & Byerlee, J. (1984). The effect of pore pressure and heating time on the strength and stability of a serpentine gouge. In *Rock mechanics in productivity and protection* (pp. 312–319). Littleton, CO: Society of Mining Engineers.

Morrow, C., Radney, B., & Byerlee, J. (1992). Frictional strength and the effective pressure law of Montmorillonite and lllite clays. In B. Evans (Ed.), *Fault mechanics and transport properties of rocks* (pp. 69–88). London: Academic Press.

Ohl, M., Plümper, O., Chatzaras, V., Wallis, D., Vollmer, C., & Drury, M. (2020). Mechanisms of fault mirror formation and fault healing in carbonate rocks. *Earth and Planetary Science Letters*, *530*, 115886. https://doi.org/10.1016/j.epsl.2019.115886

Paterson, M. S., & Wong, T.-F. (2005). *Experimental rock deformation—The brittle field*. Berlin, Heidelberg, New York: Springer Science & Business Media.

Platt, J. D., Rudnicki, J. W., & Rice, J. R. (2014). Stability and localization of rapid shear in fluid-saturated fault gouge: 2 Localized zone width and strength evolution. *Journal of Geophysical Research: Solid Earth*, *119*, 4334–4359. https://doi.org/10.1002/ 2013JB010711

Pozzi, G., De Paola, N., Holdsworth, R. E., Bowen, L., Nielsen, S. B., & Dempsey, E. D. (2019). Coseismic ultramylonites: An investigation of nanoscale viscous flow and fault weakening during seismic slip. *Earth and Planetary Science Letters*, *516*, 164–175. https://doi.org/ 10.1016/j.epsl.2019.03.042

Pozzi, G., De Paola, N., Nielsen, S. B., Holdsworth, R. E., & Bowen, L. (2018). A new interpretation for the nature and significance of mirror-like surfaces in experimental carbonate-hosted seismic faults. *Geology*, *46*(7), 583–586. https://doi.org/10.1130/G40197.1

Proctor, B., Lockner, D., Kilgore, B., Mitchell, T., & Beeler, N. (2019). Direct evidence for fluid pressure, dilatancy, and compaction affecting slip in isolated faults. *Geophysical Research Letters*, *47*, e2019GL086767. https://doi.org/10.1029/2019GL086767

Reches, Z., & Lockner, D. A. (2010). Fault weakening and earthquake instability by powder lubrication. *Nature*, *467*(7314), 452–455. https://doi.org/10.1038/nature09348

Rempe, M., Di Toro, G., Mitchell, T. M., Smith, S. A., Hirose, T., & Renner, J. (2020). *Data repository for "Influence of effective stress and pore fluid pressure on fault strength and slip localization in carbonate slip zones" M. Data, v1*. Amsterdam, The Netherlands: Mendeley Data. https://doi.org/10.17632/gvhy8kbbzb.1

Rempe, M., Smith, S., Mitchell, T., Hirose, T., & Di Toro, G. (2017). The effect of water on strain localization in calcite fault gouge sheared at seismic slip rates. *Journal of Structural Geology*, *97*, 104–117. https://doi.org/10.1016/j.jsg.2017.02.007

Rempe, M., Smith, S. A. F., Ferri, F., Mitchell, T. M., & Di Toro, G. (2014). Clast-cortex aggregates in experimental and natural calcite-bearing fault zones. *Journal of Structural Geology*, *68*, 142–157. https://doi.org/10.1016/j.jsg.2014.09.007

Rempel, A. W., & Rice, J. R. (2006). Thermal pressurization and onset of melting in fault zones. *Journal of Geophysical Research*, *111*, B09314. https://doi.org/10.1029/2006JB004314

Renner, J., & Steeb, H. (2015). Modeling of fluid transport in geothermal research. In W. Freeden, M. Nashed, T. Sonar (Eds.), *Handbook of geomathematics* (pp. 1443–1500). Berlin, Heidelberg: Springer. https://doi.org/10.1007/978-3-642-27793-1_81-2

Rice, J. R. (2006). Heating and weakening of faults during earthquake slip. *Journal of Geophysical Research*, *111*, B05311. https://doi.org/10.1029/2005JB004006

Rutter, E. H. (1974). The influence of temperature, strain rate and interstitial water in the experimental deformation of calcite rocks. *Tectonophysics*, *22*(3–4), 311–334. https://doi.org/10.1016/0040-1951(74)90089-4

Schenk, O., Urai, J. L., & Evans, B. (2005). The effect of water on recrystallization behavior and grain boundary morphology in calcite —Observations of natural marble mylonites. *Journal of Structural Geology*, *27*(10), 1856–1872. https://doi.org/10.1016/j.jsg.2005.05.015

Schmid, S., Boland, J., & Paterson, M. (1977). Superplastic flow in fine-grained limestone. *Tectonophysics*, *43*(3–4), 257–291. https://doi.org/10.1016/0040-1951(77)90120-2

Scholz, C. H. (2002). *The mechanics of earthquakes and faulting*. Cambridge, UK: Cambridge University Press. https://doi.org/10.1017/CBO9780511818516

Scuderi, M. M., & Collettini, C. (2016). The role of fluid pressure in induced vs. triggered seismicity: Insights from rock deformation experiments on carbonates. *Scientific Reports*, *6*. https://doi.org/10.1038/srep24852

Secor, D. T. (1965). Role of fluid pressure in jointing. *American Journal of Science*, *263*(8), 633–646. https://doi.org/10.2475/ajs.263.8.633

Sengers, J., & Kamgar-Parsi, B. (1984). Representative equations for the viscosity of water substance. *Journal of Physical and Chemical Reference Data*, *13*(1), 185–205. https://doi.org/10.1063/1.555708

Sibson, R. (1973). Interactions between temperature and pore-fluid pressure during earthquake faulting and a mechanism for partial or total stress relief. *Nature Physical Science*, *243*(126), 66–68. https://doi.org/10.1038/physci243066a0

Sibson, R. (1992). Implications of fault-valve behaviour for rupture nucleation and recurrence. *Tectonophysics*, *211*(1–4), 283–293. https://doi.org/10.1016/0040-1951(92)90065-E

Siman-Tov, S., Aharonov, E., Sagy, A., & Emmanuel, S. (2013). Nanograins form carbonate fault mirrors. *Geology*, *41*(6), 703–706. https://doi.org/10.1130/g34087.1

Smith, S. A. F., Bistacchi, A., Mitchell, T. M., Mittempergher, S., & Di Toro, G. (2013). The structure of an exhumed intraplate seismogenic fault in crystalline basement. *Tectonophysics*, *599*, 29–44. https://doi.org/10.1016/j.tecto.2013.03.031

Smith, S. A. F., Nielsen, S., & Di Toro, G. (2015). Strain localization and the onset of dynamic weakening in calcite fault gouge. *Earth and Planetary Science Letters*, *413*, 25–36. https://doi.org/10.1016/j.epsl.2014.12.043

Sotin, C., & Poirier, J. (1984). Analysis of high-temperature creep experiments by generalized nonlinear inversion. *Mechanics of Materials*, *3*(4), 311–317. https://doi.org/10.1016/0167-6636(84)90031-0

Spagnuolo, E., Plumper, O., Violay, M., Cavallo, A., & Di Toro, G. (2015). Fast-moving dislocations trigger flash weakening in carbonate-bearing faults during earthquakes. *Scientific Reports*, *5*(1), 16112. https://doi.org/10.1038/srep16112

Tadai, O., Tanikawa, W., Hirose, T., Sakaguchi, M., & Lin, W. (2009). *Design of new frictional testing machine for shallow fault materials* (Abstract T41A-2003). Paper presented at AGU Fall Meeting Abstracts, American Geophysical Union, Washington, DC.

Tanikawa, W., Mukoyoshi, H., & Tadai, O. (2012). Experimental investigation of the influence of slip velocity and temperature on permeability during and after high-velocity fault slip. *Journal of Structural Geology*, *38*, 90–101. https://doi.org/10.1016/j.jsg.2011.08.013

Tisato, N., Di Toro, G., De Rossi, N., Quaresimin, M., & Candela, T. (2012). Experimental investigation of flash weakening in limestone. *Journal of Structural Geology*, *38*, 183–199. https://doi.org/10.1016/j.jsg.2011.11.017

Ventura, G., & Di Giovambattista, R. (2013). Fluid pressure, stress field and propagation style of coalescing thrusts from the analysis of the 20 May 2012 M_L 5.9 Emilia earthquake (Northern Apennines, Italy). *Terra Nova*, *25*(1), 72–78. https://doi.org/10.1111/ter.12007

Verberne, B., Spiers, C., Niemeijer, A., De Bresser, J., De Winter, D., & Plümper, O. (2014). Frictional properties and microstructure of calcite-rich fault gouges sheared at sub-seismic sliding velocities. *Pure and Applied Geophysics*, *171*(10), 2617–2640. https://doi.org/10.1007/s00024-013-0760-0

Verberne, B. A., Plümper, O., de Winter, D. M., & Spiers, C. J. (2014). Superplastic nanofibrous slip zones control seismogenic fault friction. *Science*, *346*(6215), 1342–1344. https://doi.org/10.1126/science.1259003

Violay, M., Di Toro, G., Nielsen, S., Spagnuolo, E., & Burg, J. P. (2015). Thermo-mechanical pressurization of experimental faults in cohesive rocks during seismic slip. *Earth and Planetary Science Letters*, *429*, 1–10. https://doi.org/10.1016/j.epsl.2015.07.054

Violay, M., Nielsen, S., Gibert, B., Spagnuolo, E., Cavallo, A., Azais, P., et al. (2014). Effect of water on the frictional behavior of cohesive rocks during earthquakes. *Geology*, *42*(1), 27–30. https://doi.org/10.1130/G34916.1

Violay, M., Nielsen, S., Spagnuolo, E., Cinti, D., Di Toro, G., & Di Stefano, G. (2013). Pore fluid in experimental calcite-bearing faults: Abrupt weakening and geochemical signature of co-seismic processes. *Earth and Planetary Science Letters*, *361*, 74–84. https://doi.org/10.1016/j.epsl.2012.11.021

Violay, M., Passelegue, F., Spagnuolo, E., Di Toro, G., & Cornelio, C. (2019). Effect of water and rock composition on re-strengthening of cohesive faults during the deceleration phase of seismic slip pulses. *Earth and Planetary Science Letters*, *522*, 55–64. https://doi.org/10.1016/j.epsl.2019.06.027

Wagner, W. (2009). Software for the calculation of thermodynamic properties for a great number of substances, FLUIDCAL. Retrieved from http://www.thermo.ruhr-uni-bochum.de/en/prof-w-wagner/software/fluidcal.html

Wagner, W., & Pruß, A. (2002). The IAPWS formulation 1995 for the thermodynamic properties of ordinary water substance for general and scientific use. *Journal of Physical and Chemical Reference Data*, *31*(2), 387–535. https://doi.org/10.1063/1.1461829

Walker, A., Rutter, E., & Brodie, K. (1990). Experimental study of grain-size sensitive flow of synthetic, hot-pressed calcite rocks. *Geological Society, London, Special Publications*, *54*(1), 259–284. https://doi.org/10.1144/GSL.SP.1990.054.01.24

Wibberley, C. A. (2002). Hydraulic diffusivity of fault gouge zones and implications for thermal pressurization during seismic slip. *Earth, Planets and Space*, *54*(11), 1153–1171. https://doi.org/10.1186/BF03353317

Yao, L., Ma, S., Chen, J., Shimamoto, T., & He, H. (2018). Flash heating and local fluid pressurization lead to rapid weakening in water-saturated fault gouges. *Journal of Geophysical Research: Solid Earth*, *123*, 9084–9100. https://doi.org/10.1029/2018JB016132